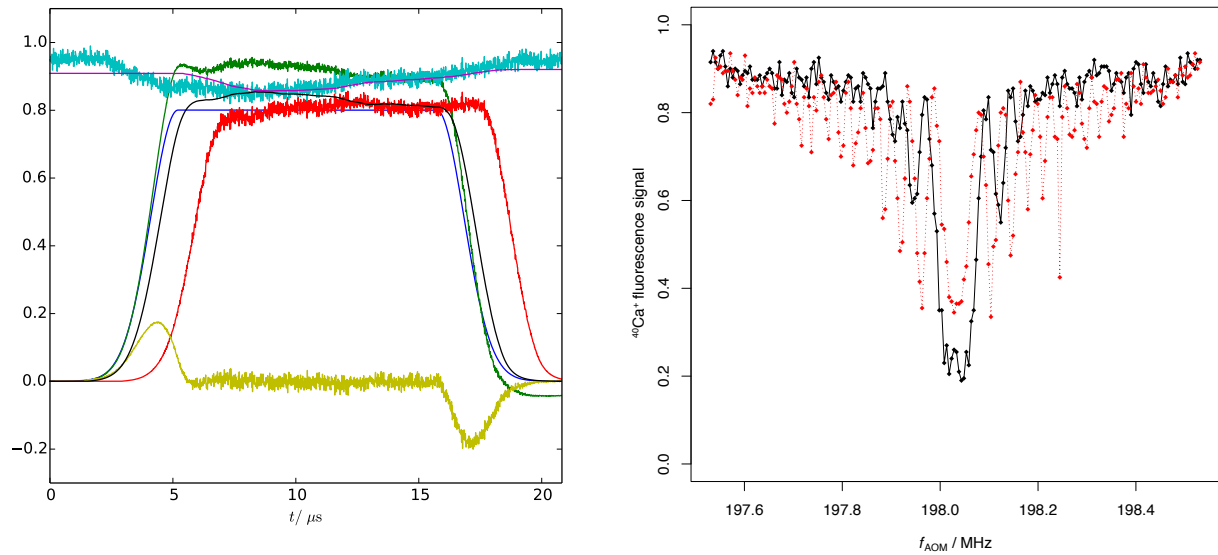


Laser Intensity Stabilization and Pulse Shaping for Trapped-Ion Experiments using Acousto-Optic Modulators

Physics BSc Semester Project



David Nadlinger

supervised by
Ludwig de Clercq

Fall Semester 2013
Trapped Ion Quantum Information Group
ETH Zürich

Abstract

This report describes the development of components for a laser intensity stabilization and pulse shaping setup for use in trapped ion quantum information experiments. A radio-frequency mixer circuit for driving the accusto-optic modulator used to modulate the laser intensity is designed. A combination of proportional-integral controller and arbitrary waveform generator is implemented on a field-programmable gate array (FPGA) to generate the pulses, and potential extensions to this basic scheme are discussed. Finally, preliminary results on the achieved noise reduction and the effect of pulse shaping on the gate pulses for the 729 nm $|4^2P_{1/2}, m = 1/2\rangle \leftrightarrow |3^2D_{5/2}, m = 3/2\rangle$ carrier transition in $^{40}\text{Ca}^+$ ions confined in a linear Paul trap are presented.

Contents

1. Introduction	5
2. Background	6
2.1. Optical Quantum Gates in Trapped Ions	6
2.2. Acousto-Optic Modulators	7
2.3. Intensity Feedback and Pulse Shaping	8
3. RF Modulation Circuit	10
3.1. Circuit Design	11
3.1.1. Analog Multiplier IC Evaluation	11
3.1.2. RF Input/Output	12
3.1.3. Control Input	12
3.1.4. Power Supply	13
3.2. PCB Layout	13
3.3. Performance Characteristics	15
3.3.1. RF Network Parameters	15
3.3.2. Noise Performance	16
3.3.3. Control Input Linearity	18
3.3.4. Control Input Transfer Function	19
3.3.5. RF Feedthrough and Output Offset	20
4. FPGA-based PID Controller	21
4.1. Control Theory Fundamentals	21
4.1.1. Feedback Control	22
4.1.2. PID(F) Control	23
4.1.3. Discrete Time Representation	24
4.2. Modelling the AOM Input Power to Laser Intensity Relation	26
4.3. Smith Predictors	27
4.4. Simulation Results	28
4.5. The EVIL Controller	30
4.5.1. PIDF and Smith Predictor Implementation	31
5. Results	33
5.1. Noise Rejection Bandwidth	33
5.2. Pulse Shaping Results	34
6. Conclusion	36
A. AOM Response Measurements	37
A.1. Open-Loop Frequency Response	37
A.2. AOM Latency	39

B. DIRE RF Multiplier Assembly and Setup	41
B.1. Function Summary	41
B.2. Configuring the DIRE Board for Use with the EVIL Controller	41

1. Introduction

Both in research regarding fundamental properties of quantum-mechanical systems (such as decoherence or methods for state control) and in investigations concerned with potential avenues towards a scalable universal quantum computer [1], atomic ions in electromagnetic traps have been one of the most intensely studied systems over the last decade.

In typical experiments, one or more ionized atoms are confined in a region of space using a combination of static (DC) and time-dependent (radio-frequency, RF) electrical potentials. Several types of laser cooling are employed to bring the ions into or close to their motional ground state. By applying suitable optical fields, the internal energy levels of an ion can be coupled to its motional states, and thus via Coulomb interaction also to other ions in the trap. Quantum gates are then implemented by applying optical or microwave dipole forces that depend on the qubit state of the ions. [2] To implement optical quantum gates with a high fidelity while avoiding to heat the system by exciting unwanted transitions, it is essential that the properties of the laser light incident on the ions are precisely controlled, in terms of frequency and phase as well as intensity.

Within the scope of this project, a scheme for stabilizing the intensity of the laser pulses used for implementing quantum gates by means of a feedback loop was investigated. The main goal initially was to design and build a device for amplitude modulation of an electrical RF signal. After assembling the printed circuit board and characterizing its performance properties, the dynamic characteristics of the acousto-optic modulators (AOMs) used for modulating the light intensity were investigated. A spline-based arbitrary waveform generator was integrated with a loop controller and triggering capabilities on an FPGA-based platform, and several possible control schemes were analyzed.

Chapter 2 briefly discusses the physical phenomena underlying quantum information processing in ion traps as relevant to this project, and the working principle of AOMs. It also provides a high-level view of the control loop employed for intensity stabilization and pulse shaping.

In chapter 3, the engineering process behind the *DIRE* RF modulation device is described, which originally was the main focus of this project, and an evaluation of its performance characteristics in isolation is presented.

Chapter 4 begins with a review of the basics of single-input-single-output system control theory, before discussing a few control algorithms and their realization in a digital discrete-time hardware environment. Numerical simulations are performed to compare the different approaches as applied for laser pulse shaping using the framework described in the rest of the report. In the second part of the chapter, the architecture of the pulse shaping firmware for the FPGA platform is described.

In chapter 5, some preliminary performance results for the complete intensity stabilization loop are presented. This includes measurement on the frequency-dependent noise rejection profile of the loop, and data on the effect of a smooth laser pulse envelope on the response of a trapped $^{40}\text{Ca}^+$ ion. However, the more advanced control schemes presented in chapter 4 could not be implemented in the scope of this project.

Finally, chapter 6 concludes the report.

Appendix A describes supplementary measurements on the dynamics of two particular AOM models. To aid in setting up an intensity stabilization/pulse shaping control loop in a typical experimental setup, appendix B contains further details on the developed RF multiplier circuit and a suggestion for a step-by-step adjustment procedure.

2. Background

2.1. Optical Quantum Gates in Trapped Ions

In trapped ion quantum information, a combination of DC and RF fields is used to create a three-dimensional pseudo-harmonic potential, into which one or more atomic ions are loaded. In the Trapped Ion Quantum Information Group at ETH Zürich, the ion species employed are $^{40}\text{Ca}^+$ and $^9\text{Be}^+$.

The experiments on actual ions conducted as part of this project were concerned with $^{40}\text{Ca}^+$. Its electronic level structure in a magnetic field of $B = 11.964$ mT is shown in figure 2.1.¹ The two qubit states are generally chosen such as to yield an effective two-level system with a long lifetime. In $^{40}\text{Ca}^+$, the quadrupole transition at 729 nm between the $|\downarrow\rangle = |4^2P_{1/2}, m = 1/2\rangle$ and $|\uparrow\rangle = |3^2D_{5/2}, m = 3/2\rangle$ states fits this requirement well. The short-lived dipole transition at 397 nm can be used both for Doppler-cooling and for detecting occupation of the $|\downarrow\rangle$ state using state-dependent fluorescence. [4]

The fact that incident radiation also couples to the motional states of the ion in the harmonic potential further complicates the interactions and thus the level structure. To the right of figure 2.1, the composite system consisting of internal state and motional degree of freedom is shown. The single transition between the qubit levels is split into three transitions separated by the trap frequency ω_f , the *carrier* $|\downarrow, n\rangle \leftrightarrow |\uparrow, n\rangle$, the *red sideband* $|\downarrow, n\rangle \leftrightarrow |\uparrow, n - 1\rangle$ and the *blue sideband* $|\downarrow, n\rangle \leftrightarrow |\uparrow, n + 1\rangle$. [2]

In the interaction picture and the Lamb-Dicke regime, where the spatial extent of the harmonic oscillator wave function is small compared to the wavelength of light, the Hamiltonian for resonant excitation of the carrier transition can be written as

$$H_I = \frac{\hbar}{2} \Omega (\sigma^+ + \sigma^-). \quad (2.1)$$

If this Hamiltonian is applied continuously, Rabi oscillations are observed between the two internal qubit states, with frequency Ω . For a given laser frequency, this *Rabi frequency* depends linearly on the intensity of the incident light. Considering a single-qubit rotation realized by a laser pulse of length T tuned to the carrier frequency, the angle of rotation of the Bloch sphere ϑ incurred by applying this Hamiltonian is thus proportional to the integral of the intensity,

$$\vartheta \propto \int_0^T I(t) dt, \quad (2.2)$$

or simply the area of the pulse in an intensity-time graph. To implement quantum gates with high fidelity, it is thus important to be able to precisely control the intensity of the laser pulses used. The fact that the action of the gate depends in good approximation only on the integral of the laser power incident at the transition frequency also opens the door towards optimizations of the pulse shape regarding other criteria.

¹The precise value of the magnetic field strength is essentially arbitrary if only $^{40}\text{Ca}^+$ is considered. It is, however, an attractive choice for our $^9\text{Be}^+$ qubit, as the transition between the two chosen hyperfine qubit states is field-independent to first order at this value.

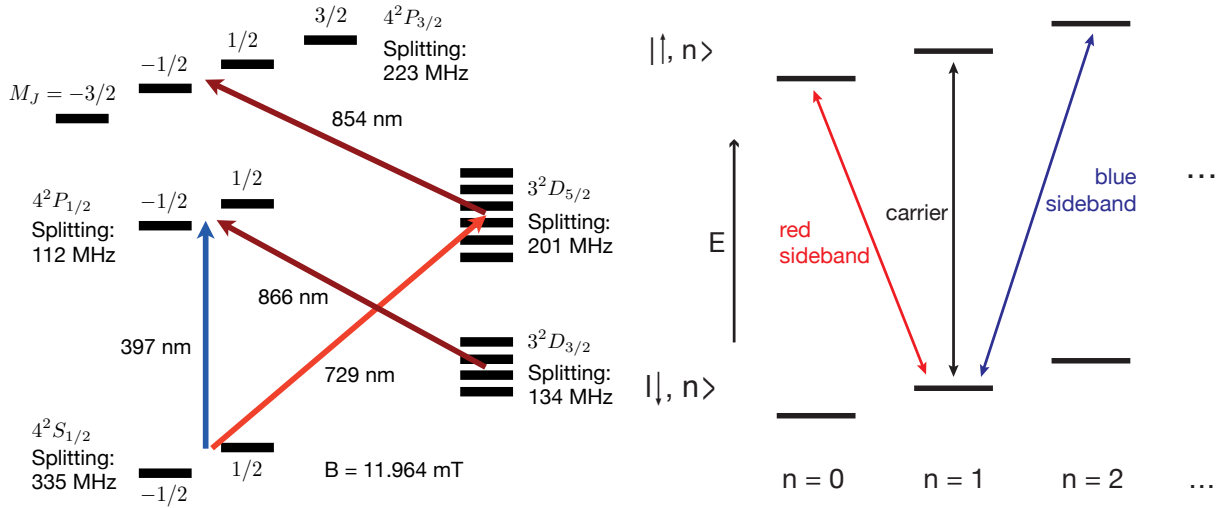


Figure 2.1.: Level structure of a $^{40}\text{Ca}^+$ ion in a harmonic trap potential. *Left:* The internal electronic level structure with the 729 nm qubit transition. [3] *Right:* Schematic representation of this carrier transition and the two sidebands in the composite system of internal and motional states.

Similar considerations also apply to the sidebands. The coupling of detuned beams to the motional state enables the realization of multi-qubit gates mediated by the Coulomb interaction between different ions in the same trap potential (see e.g. [5]).

As far as the experimental implementation of quantum gates is concerned, it is desirable that both the frequency and the duration of the laser pulses can be quickly fine-tuned in a way that is amenable to automatic calibration, as the exact transition frequency depends on the magnetic field and the total available laser power might fluctuate over time.

2.2. Acousto-Optic Modulators

A class of devices often used where fast precision control of laser beams is required are acousto-optic modulators (AOMs). They are based on the phenomenon that sound waves travelling in a transparent medium locally change its refractive index. An electro-acoustic transducer, typically based on the piezo-electric effect is attached to one side of a suitable medium, forming a *Bragg cell*. If a sound wave is applied, regions of alternating optical density form. As the frequency of the incident light ω is usually much smaller than the sound frequency Ω , it is possible to treat the interaction as Bragg diffraction off a grating [6], as depicted in figure 2.2.

The Bragg condition for constructive interference is

$$\sin \theta = \frac{\lambda}{2\Lambda}, \quad (2.3)$$

where $\lambda = \frac{2\pi c}{n\omega}$ is the wavelength of the light and $\Lambda = \frac{2\pi u}{\Omega}$ that of the sound wave.

The reflected wave will be slightly shifted in frequency, $\omega_r = \omega \pm \Omega$. This can be visualized as Doppler shift caused by the moving planes of reflection. The transmitted light is usually referred to as the 0^{th} -order beam, whereas the main reflected beam is referred to as the $\pm 1^{st}$ -order beam (depending on the sign of the frequency shift, i.e. the orientation of the incident beam compared to the travel direction of the sound waves). Due to the finite extent of the beam, higher-order diffracted beams of greatly reduced intensity will also occur.

The fraction of first-order diffracted light to the total incident power, R , depends on the magnitude of the change in refractive index. The latter is in turn proportional to the square root of the

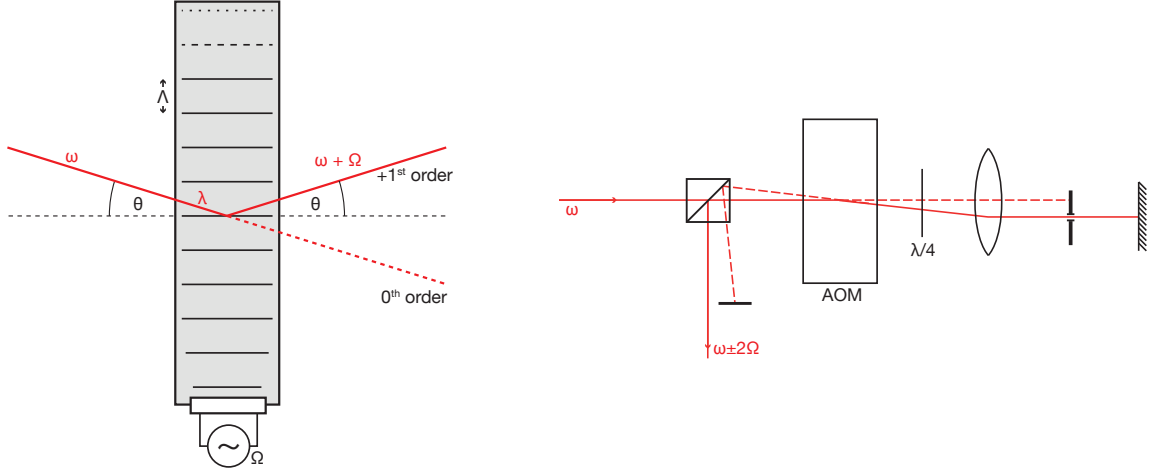


Figure 2.2.: *Left:* Working principle of an accusto-optic modulator. Sound waves in a medium create fluctuations in optical density, which lead to Bragg refraction. *Right:* AOMs are frequently used in double-pass configuration.

intensity of the sound wave I_S . Accounting for saturation effects, the relation of diffraction efficiency to acoustic power can be written as

$$R \propto (\sin \sqrt{I_S})^2, \quad (2.4)$$

i.e. for small powers I_S , the intensity of the refracted beam can be controlled linearly by modulating the intensity of the electrical drive signal for the piezo transducers. R is also referred to as *diffraction efficiency*. [6, 7]

The response to changes in the RF intensity is not instant, however. Two main effects are relevant here: First, the density wave takes a certain amount of time to travel from the transducers at the edge of the cell medium to the location of the laser beam. This leads to a constant time delay the response which depends on the speed of sound in the diffracting medium and the distance from the transducers to the optical aperture. Second, the fact that the acoustic wave front takes a finite amount of time to cross the waist of the incident beam of light means that the intensity response to changes in acoustic power will effectively be low-pass filtered. The extent of this effect will again depend on the speed of sound and the diameter of the beam. [7]

The frequency shifting property of AOMs is particularly useful to generate several detuned beams (e.g. to address the motional sidebands in addition to a resonant beam) from a single laser source. It is also employed for fast and reliable fine-tuning of the laser frequencies, as the laser itself is usually frequency-locked by referencing the wave length of its output to a highly stable reference cavity.

To increase the frequency bandwidth addressable via a single device and to keep the first-order diffracted beam at the same angle irrespective of operation frequency, AOMs are often used in a double-pass configuration. Here, the desired reflection order is selected at the exit port of the AOM using an aperture and retro-reflected back into the AOM. The final beam, which has been shifted by twice the frequency f_{AOM} and attenuated by a factor of R^2 can then be selected using e.g. a polarizing beam-splitter. An example for such a configuration is shown in figure 2.2. [8]

2.3. Intensity Feedback and Pulse Shaping

In the above, the need for precise control over the intensity of laser pulses for ion trap quantum information experiments was described. Given that a certain diffraction efficiency of an AOM effectively acts as a multiplicative factor to the laser intensity at its input, intensity noise coming from the laser source is also present on the gate pulse. Additionally, fluctuations in the optical

density of air along the path through the different parts of the trapping setup contribute significantly to variations in the effective laser intensity levels.

Since these effects are generally random in nature, the basic idea of any intensity stabilization scheme will be to measure the actual laser intensity at a position as close to the trapping zone as possible, continuously adjusting the power to keep it as close as possible to the desired value by means of a feedback loop. In the experimental setup that was the primary target of this project, this is achieved by a photodiode positioned at a pick-off immediately before the beams enter the vacuum system housing the 3D Paul trap.

In the simplest case, such a control system would try to hold the laser intensity at a fixed target value as long as some external trigger signal is present, effectively creating a square pulse. However, considering that the goal in typical quantum information experiments is to exclusively address a single, narrow transition, this might not be optimal:

As a simple example, consider a simple square pulse,

$$A(t) = \frac{1}{T} \left(\Theta(t - \frac{T}{2}) - \Theta(\frac{T}{2} - t) \right) \quad (2.5)$$

with Fourier spectrum

$$A(\omega) = \frac{1}{\sqrt{2\pi}} \frac{1}{T} \int_{-\frac{T}{2}}^{\frac{T}{2}} e^{-i\omega t} dt = \frac{1}{\sqrt{2\pi}} \text{sinc}\left(\frac{T\omega}{2}\right). \quad (2.6)$$

In a typical experiment, a gate pulse might be of duration $T = 5 \mu\text{s}$. The FWHM of the power spectrum $|A(\omega)|^2$ of this envelope then is 177 kHz. The actual bandwidth of the pulse would certainly be lower in an experiment due to the rise time of the AOM and other electronics involved. Still, comparing this estimate to the typical line width of ultra-stable laser systems in the low kHz region suggests that the finite length of the pulse has a non-negligible effect on the frequency selectivity of the gate pulses.

If precise control over the envelope waveform for the gate pulses can be achieved, the envelope can be adapted to a shape that produces a narrower spectrum, for example a Gaussian bell curve. If there are any narrow unwanted transitions near the target frequency, it would even be possible to craft a pulse shape with a frequency spectrum specifically designed to avoid exciting them.

3. RF Modulation Circuit

As discussed in section 2.2, in order to use AOMs for intensity modulation it is necessary to control the amplitude of an RF signal. In the most basic case, on/off control, this can be done using a simple RF switch, and in fact, such a configuration¹ is currently used in a number of places in the experiments of the group. Before the start of the project, first pulse shaping experiments had already been conducted using a passive diode ring mixer². However, its linearity imperfections gave rise to an undesirable level of distortion, and its small linear range of approx. 0.3 V was difficult to accommodate with regards to noise. It was thus chosen to build a prototype for investigating the applicability of active analog multiplier ICs in this scenario.

In the following, the target specifications are summarized, before briefly discussing circuit design, PCB layout and the performance characteristics of the assembled device, which has been nick-named *DIRE*.

RF input: The AOMs in the beam paths that are potential use cases for the control loop were all operated in the 60 to 200 MHz region. A -3 dB bandwidth of 80 MHz was considered the absolute minimum to handle at least some of the AOMs, with 150 MHz being enough for use in current setups and > 250 MHz leaving enough headroom for the circuit to be useful for any potentially similar applications in the future. As the output power/attenuation of the RF sources used in the laboratory is programmable, the precise RF input power required for optimal operation was not specified, though it was desirable for the circuit to perform well between 0 and 5 dBm of input power for ease of integration with existing setups.

Control input: For the PID controller hardware, a maximum effective bandwidth of 500 kHz was estimated from previous transfer function measurements, so the usable input frequency range was required to be DC to 500 kHz. To attenuate high frequency noise picked up from the environment, an appropriate low-pass filter was to be included in the control input path, should the design found be capable of accommodating faster control signals. An input range of at least 0 to 1 V was found desirable for a low-noise connection to the controller hardware, with the response being as linear as possible.

RF output: In the final setup (see e.g. figure 5.2) the output of the mixer is connected to an RF power amplifier with a gain of +29 dBm min., +34 dBm typ. Given the level of power required for the used AOMs to reach maximum diffraction efficiency, this equates to a target (minimum) full-scale output power of 3 to 4 dBm to avoid having to use additional amplification. As customary for RF lab equipment, the target output impedance was 50Ω .

Power supply: Several pieces of equipment in the lab, including the PID controller used in the target setup, use ± 15 V DC supply rails. It was thus desirable to find a way to drive the multiplier circuitry from this source or the 24 V rail required for the RF power amplifier to decrease power supply proliferation. Switched mode voltage conversion was to be avoided for fear of (radiated) noise.

Environment: The circuit was designed as a prototype with a typical laboratory environment in mind, so temperature, humidity and similar environmental factors could be assumed to be in a moderate range. High-power RF circuitry is used in the vicinity of the setup (for the RF trap drive), so at least the keeping the possibility to add a proper enclosure for shielding later was desirable.

¹Based on e.g. the Mini-Circuits ZASW-2-50DR+ single-pole-double-throw switch, its TTL input being connected to the central control system.

²Specifically, the Mini-Circuits ZLW-3+ 0.025 to 200 MHz frequency mixer.

Noise: The most prominent noise sources in the rest of the target setup were estimated to be the quantization effects of the 10 bit ADCs/DACs in the PID controller used, the photodiode used for feedback and the RF signal source itself. Avoiding to add any significant amount of noise in the mixer to that seemed feasible. An output noise floor of at least 65 dBm below the carrier was thus a design goal.

3.1. Circuit Design

In this section, a number of design decisions made while designing the RF multiplier circuit are outlined. For details on the finished circuit, please refer to appendix B.

3.1.1. Analog Multiplier IC Evaluation

Most of the design choices are centered around the mixer chip used. Several ICs were initially considered for this:

- *Texas Instruments MPY634* [9]: This chip originally manufactured by Burr-Brown is inexpensive, requires a minimum of external components and has a large output voltage range. However, its (-3 dB) bandwidth of *DC* to 10 MHz is not sufficient for this application, and it also requires rather high supply voltages (although this fact alone would have not been an issue in this particular application due the availability of ± 15 V rails).
- *Analog Devices AD834* [10]: The AD834 four-quadrant multiplier offers > 500 MHz bandwidth, a low output offset and is available in a convenient SOIC-8 package. However, its different current mode output would require a transformer/balun to reach optimal performance and convert the ± 4 mA output current to the desired signal levels. And even if suitable 1:16 transformers are readily available from a number of specialized suppliers such as Mini-Circuits, Inc., using this chip would have meant to include a BOM item that cannot easily be sourced from common distributors like Farnell. Another option might be to use an op-amp circuit or a specialized line-receiver IC for different-to-single-ended conversion with an appropriate gain, but the bandwidth of the AD834 would likely have been difficult to maintain this way.
- *Analog Devices AD835* [11]: This chip is similar to the AD834, with a lower bandwidth of 250 MHz, but featuring a single-ended voltage-mode output. It is also available in a SOIC-8 package.
- *Analog Devices ADL5391* [12]: The ADL5391 is from a newer generation than the other ICs and offers superior bandwidth (2 GHz) and noise performance. It also comes with an internal voltage reference, allowing operation off a single supply rail. Its differential output operates in voltage-mode with an output swing of ± 2 V, making it easy to offer a properly terminated $+10$ dBm output. However, it is only available in a 16-lead LFCSP package, which is hard to solder without using a reflow process.

Due to manufacturability concerns – initially, it was not clear if the prototype PCBs would need to be etched in-house, thus precluding the use of solder-mask and a larger number of PCB vias – it was decided to pursue a design based on the conveniently packaged AD835, even though it is slightly more expensive than the ADL5391 and there would not be much headroom in terms of bandwidth and output power.

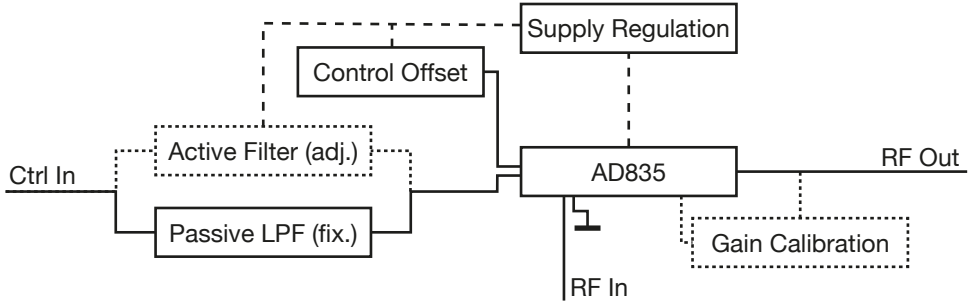


Figure 3.1.: Overview of the DIRE RF multiplier circuit. The dotted lines indicate components not present in the default configuration: Instead of the passive low-pass filter (LPF) on the control input, an active second-order filter with adjustable zero and gain can be chosen. At the output, extra feedback resistors can be inserted to fine-tune the multiplier gain.

3.1.2. RF Input/Output

The RF side of the circuit was kept as simple as possible to avoid the need for complex techniques in the layout phase. The RF input is coupled in via a 10 nF capacitor to block DC content and terminated by a $49.9\text{ }\Omega$ resistor at the Y input of the multiplier chip, which was selected for the better RF feedthrough performance. The corner frequency of the resulting first-order high-pass filter is given by (see e.g. [13])

$$f = \frac{1}{2\pi RC}, \quad (3.1)$$

which evaluates to $f = 318\text{ kHz}$ using the above parameters. This is considerably smaller than the frequency of the RF signals in the 100 MHz region used in AOM applications.

The AD835 provides a low-impedance voltage-mode output, so the output stage merely consists of a $49.9\text{ }\Omega$ resistor to provide proper back-termination. An optional resistive divider allows to feed back a portion of the output signal to the otherwise unused summing input of the chip for fine adjustment of the multiplier divisor, as suggested in the manufacturer data sheet. These components are expected to be left out in a typical configuration for experiments in the group, as the scaling calibration can just be performed in the control signal source and increasing the gain of the chip-internal op-amp output stage results in a reduced bandwidth.

3.1.3. Control Input

For the control input filter, a second-order RLC low-pass filter in Butterworth configuration was chosen. The component values were obtained by requiring the DC (i.e., pass-band) resistance to be approximately $50\text{ }\Omega$. Based on estimations regarding the maximum control bandwidth of an intensity stabilization loop and the typical rise time limit of AOMs, two versions were initially built up: One with a corner frequency of 1 MHz to not negatively impact the control loop bandwidth even under optimistic assumptions, and a second one with the cut-off at 10 MHz to make the impact on the AOM rise time negligible for open-loop applications. The component choices suggested in appendix B correspond to a corner frequency of 3 MHz to achieve a good trade-off between AOM rise time and susceptibility to high-frequency noise.

As an extension to be able to directly use the device in a future fiber laser noise reduction setup, an additional active filter circuit (specified by Vlad Negnevitsky) was also included. It implements a variable-gain second order filter with an adjustable zero and an adjustable pole. See the schematic in appendix B for details.

The input stages offered by the AD835 multiplier are differential. The additional input was used to provide an variable input offset for the user to be able to adjust the zero point to the specific device

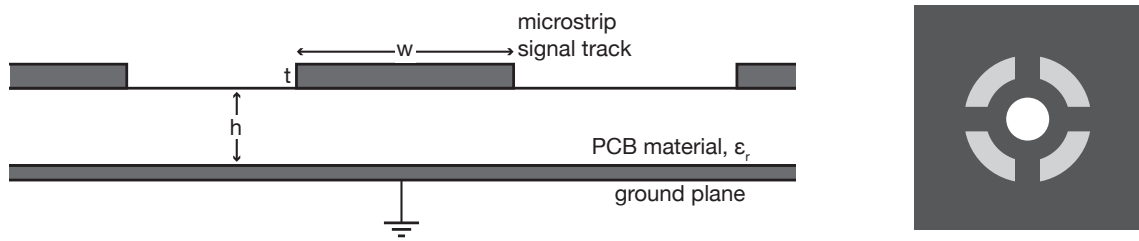


Figure 3.2.: *Left:* Geometry of microstrip PCB track transmission line. *Right:* Example of thermal relief pad design. The four thin connections between the copper pad and a large ground plane inhibit the heat transfer, making it easier to solder a connection at the central drill hole.

generating the control input, and to correct for the residual input offset voltage of the multiplier chip. This is also an useful adjustment for the optional on-board filter circuit, and additionally allows for easier testing, as no external low-noise voltage source is required for RF measurements.

3.1.4. Power Supply

In terms of noise performance, the AD835 specifications quote a noise floor of $50 \text{ nV}/\sqrt{\text{Hz}}$. To fully exploit this potential, a power supply with appropriately low noise levels is needed. To meet this specification, and also for ease of use with existing power supplies in the lab, it was decided to include local voltage regulation on the multiplier board. The maximum quiescent current for the AD835 is specified at 25 mA. Based on an output power of +7 dBm into a 50Ω load, a worst-case power consumption of 60 mA was estimated. Another 30 mA for the active filter circuit yielded a minimum power supply rating of 100 mA, with the intention of including enough reserves to keep heating low.

Based on this, several types of voltage regulators were investigated. As mentioned above, switched-mode designs were ruled out early in the process for the relative difficulty of designing the circuit so as to avoid emitting switching mode noise. As power efficiency was of no concern beyond possible heating issues and the required currents are relatively low, simple linear regulators are well-suited for the application. Initially, several low-noise low-dropout regulator ICs were investigated. However, it was found that negative types were much less readily available than positive regulators, and expect for a few modern, rather expensive ICs, their noise performance was hardly better than of standard (non-low-dropout) 78xx/79xx-series voltage regulators.

In the end, a simple design based on the ON SEMICONDUCTOR MC78M/MC79M-series regulators was chosen. In accordance with the data sheets for the multiplier chip and high-speed op-amp layout practice a combination of 10 nF ceramic and 10 μF bypass tantalum capacitors was used at all IC power supply pins, with ferrite beads used to avoid any resonance behavior in the supply paths. Due to the small size of the circuit and the resulting small parasitic inductances in the finished PCB layout this is likely to be over-cautious design. It was planned to remove the bypassing components one by one while monitoring the RF response on a prototype board to determine their necessity, but the experiments were not carried out to this date, as no further batch of multiplier boards was built beyond what was initially planned.

3.2. PCB Layout

In creating printed circuits for RF applications, a central aspect is that at higher frequencies, PCB tracks can no longer be regarded as ideal connections between lumped-element components. Instead, they act as transmission lines, and must be matched to the external inputs and outputs. For the most

common geometry, a *microstrip* line consisting of a single track on one side of the PCB above a solid ground plane on the other side (see figure 3.2), the characteristic impedance can be approximated to within 1 – 2% as

$$Z = \frac{Z_0}{2\pi\sqrt{2(1+\varepsilon_r)}} \ln \left(1 + \frac{4h}{w'} \left(\frac{14 + \frac{8}{\varepsilon_r}}{11} \frac{4h}{w'} + \sqrt{\left(\frac{14 + \frac{8}{\varepsilon_r}}{11} \frac{4h}{w'} \right)^2 + \pi^2 \frac{1 + \frac{1}{\varepsilon_r}}{2}} \right) \right), \quad (3.2)$$

where $Z_0 = 376.7 \Omega$ is the impedance of free space, ε_r the relative dielectric constant of the PCB substrate, h its thickness, and w' is the effective width of the track. [14] The latter is defined as

$$w' = w + t \frac{1 + \frac{1}{\varepsilon_r}}{2\pi} \left(1 + \ln \left(\frac{4}{\sqrt{\left(\frac{t}{h} \right)^2 + \left(\frac{1}{\pi} \frac{w+11}{t+10} \right)^2}} \right) \right), \quad (3.3)$$

where w is the actual width of the track and the second term is a correction for the finite copper thickness t . [14]

The PCB parameters as given by the prototype PCB manufacturer were: FR4 material ($\varepsilon_r = 4.5$), $h = 1.57 \text{ mm}$, 1 oz copper layer ($t = 34.8 \mu\text{m}$). Solving equation (3.2) for a target impedance of $Z = 50 \Omega$ given these values yields a track width of $w = 2.9 \text{ mm}$. This is rather large given the small overall size of the circuit. At the same time, for the operation at the moderate design frequency of $f = 250 \text{ MHz}$, the characteristic length for the occurrence of transmission length effects, as estimated based on the wavelength in copper λ , is on the order of

$$\frac{\lambda}{4} \approx \frac{1}{4} \frac{0.8c}{250 \text{ MHz}} = 24 \text{ cm.}$$

As this is considerably larger than the estimated size of the final PCB, it was decided to just try and keep the unit size to a minimum and just make the RF tracks as broad as reasonably possible within the layout.

In line with this decision, the various passive components were chosen in 0603 (1.6 mm × 0.8 mm) surface-mount packages. The small size improves the component density on the PCB, while still being easily solderable manually. In addition, the smaller size generally also decreases parasitic inductance in the component packages, which is of particular importance for high-frequency bypass capacitors. [15]

With the exception of a single small power supply trace section, the bottom side of the PCB was entirely dedicated to a ground plane. The main motivation for this was to make in-house manufacturing of a first prototype feasible, where via connections are difficult to produce. It also serves as a low-impedance return path for RF signals. However, given that the board ultimately was never manufactured manually, it might have been beneficial for the electrical performance to route a few more tracks on the bottom layer. This applies in particular to the feedback paths on the operational amplifier for the active input filter, which are critical for the filter performance, but where the design is more convoluted than necessary.

In line with common guidelines for high-speed PCB layout (see e.g. [16]), vias were placed at all ground pins of bypass capacitors to lower the inductance of the connection to the ground plane. Unfortunately, no thermal relief (see figure 3.2) was included at the respective pins, making the components harder to solder manually than necessary due to the high thermal mass of the ground plane.

On the control input side, the circuit was laid out such that the direct path to the multiplier input goes through the active input filter, as the operation frequencies are higher in this use case. The passive input filter circuitry was arranged around that, with the input inductor of the RLC

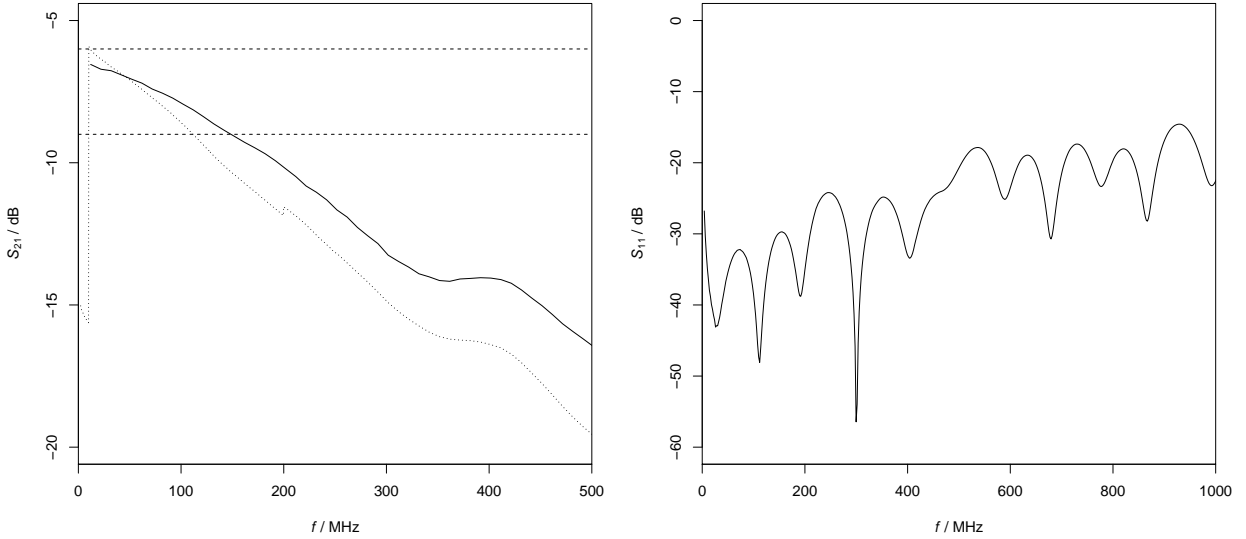


Figure 3.3.: RF response of the DIRE RF multiplier board as measured using a network analyzer. *Left:* Trasmission gain (S_{21}) at $V_{ctrl} = 1.05$ V as a function of the frequency, with the dashed horizontal lines denoting -6 dB and -9 dB. The solid line represents the data corrected by a measurement of the SMA cables used to connect the PCB to the spectrum analyzer, whereas the dotted line shows the raw data (see text). *Right:* Reflection gain (S_{11}) measurements, showing acceptable (< -30 dB) incoupling in the region of interest.

filter and a $0\ \Omega$ -resistor at its output allowing to completely disconnect the traces in the active filter configuration. The paths around the optional gain adjustment divider at the output were kept to minimum length using a similar layout. The unoccupied area on the top copper layer was dedicated to ground and negative supply voltage polygons around the positive and negative voltage regulators, respectively, for improved heat sinking.

No issues were found in the PCB design upon assembly, with one small exception: The PCB footprints for the potentiometers were drawn manually according to the manufacturer recommendations. Apparently, the dimensions in the data sheet were optimized strictly for a reflow soldering process, as they turned out to only extend beyond the potentiometer casing by a small margin. This makes contacting the pads on the bottom of the potentiometers more difficult than necessary when manually assembling the board.

3.3. Performance Characteristics

In this section, the measurements performed to characterize the assembled RF multiplier boards in isolation are described.

3.3.1. RF Network Parameters

An important part in evaluating the suitability of the DIRE board design was to verify whether it would operate correctly at the RF carrier frequencies used in the target AOM setups. For this, a board was connected to a two-channel bench power supply set to ± 7 V DC. For ease of measurement, a $50\ \Omega$ terminator was attached to the control input and the offset potentiometer was adjusted for an effective control voltage of $V_{ctrl} = 1.05$ V, which nominally corresponds to unity gain of the multiplier chip. The RF input and output were then connected to an AGILENT *FieldFox N9912A* handheld spectrum analyzer used in network analyzer mode.

The network parameter measurements were performed with an IF bandwidth of 3.00 kHz and the *HIGH* output power setting (+6 dBm nominal) with the results being shown in figure 3.3.

The left graph shows the transmitted RF power, i.e. the S_{21} parameter. The raw data, which is plotted as a dotted line, shows several unexpected features. The first is a sudden 10 dB drop of the measured gain below 10 MHz. The two closest measured samples are a gain of -15.62 dB at 9.936 MHz and a gain of -5.91 dB at 10.194 MHz. There is no obvious physical interpretation of this, as the input low-pass filter cutoff is much lower (see eq. (3.1)), and indeed the gain again rises towards lower frequencies. Combined with the fact that the break seems to occur exactly at 10 MHz, the most likely interpretation is an issue with e.g. frequency range switching within the network analyzer. A similar, albeit smaller (only 0.4 dB in magnitude) discontinuity occurs also at 199.8 MHz, which most likely is also just a measurement artefact.

This hypothesis is also corroborated by a measurement of the parameters of the SMA cables used to connect the network analyzer to the device under test (approx. 2.5 m in length), with an SMA I connector taking the place of the EVIL board. The same features were observed, along with an over-emphasis of the frequency region below approximately 50 MHz ($S_{21} > 0$ dB) and a noticeable roll-off towards higher frequencies. The solid line shows the S_{21} data for the DIRE board with this calibration measurement subtracted.

The maximum transmission gain measured was -6.5 dB. The $1 : 1$ voltage divider formed by the 50Ω output resistor and the connected load yields a theoretical best case result of

$$S_{21} = 10 \text{ dB} \cdot \log_{10} \left(\left(\frac{1}{2} \right)^2 \right) = -6.02 \text{ dB},$$

(assuming exactly unity gain at the multiplier chip), so the measured result is within the expected range. The 0.5 dB in unaccounted losses are likely caused by the non-ideality of the PCB traces, small losses at the PCB-mounted connectors, etc.

The dashed lines in the plot correspond to gains of -6 dB and -9 dB, with the latter intersecting the measurement results at 149 MHz, which means that the 3 dB gain flatness target of 150 MHz has been reached if the constant losses are considered. At 200 MHz, the gain is still -10.1 dB. This is enough for practical applications, considering that the multiplier chip can handle gains slightly larger than unity (see next section).

As the 50Ω input via the SMA socket is not matched well to the traces on the PCB, it is difficult to predict the exact behavior of the reflection (i.e. S_{11}) parameter. However, as outlined in the previous section, for lower frequencies the match should be acceptable, whereas for higher frequencies, a significant amount of reflections is expected. This is observed in the measurement (right plot in figure 3.3). While the incoupling quality indeed deteriorates for higher frequencies, in the frequency regions where the device is going to be used, i.e. up to approximately 200 MHz, S_{11} is below -30 dB, which can be considered sufficient for most applications.

3.3.2. Noise Performance

As briefly mentioned above, with the target application of the multiplier board being in laser noise reduction, it is crucial that the board itself does not significantly increase the noise levels beyond what is already present in the system. Because the diffraction efficiency of the AOM that is controlled via the RF multiplier depends on the power level of the RF carrier, the most interesting noise figure is that of amplitude modulation of the carrier. As

$$\sin(\omega t) \sin(\Omega t) = \frac{1}{2} (\cos((\Omega - \omega)t) - \cos((\Omega + \omega)t)),$$

such amplitude modulation appears as additional sidebands in the frequency spectrum.

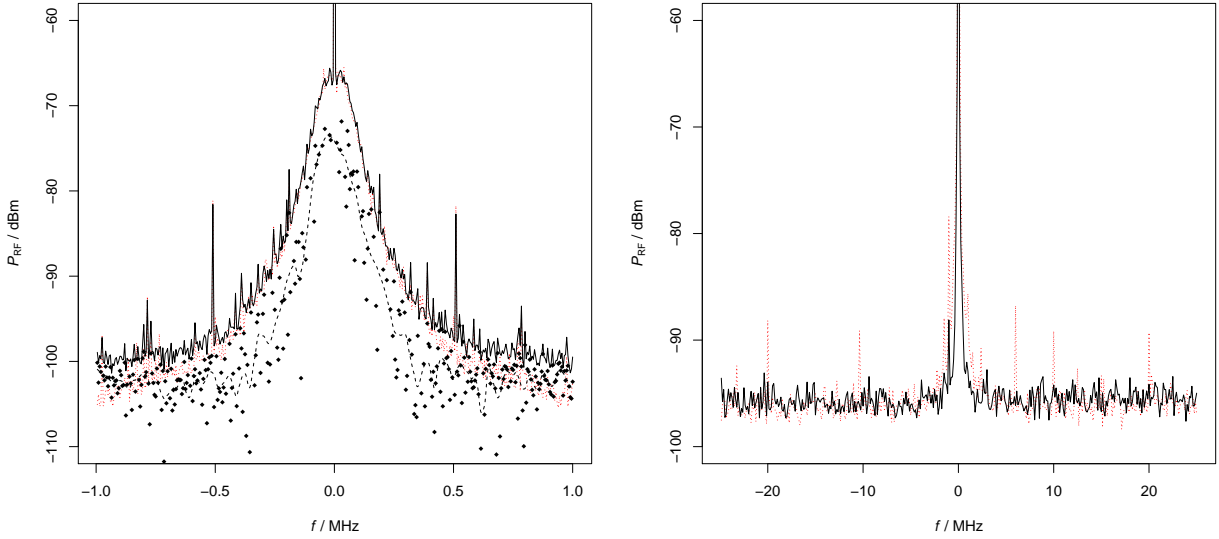


Figure 3.4.: DIRE PCB noise measurements. *Left:* RF power spectrum with a resolution bandwidth of 10 Hz (401 points). The dashed red line corresponds to the signal directly after the RF source, the solid black line to the DIRE output, with both curves normalized to 0 dBm carrier amplitude. The black dots denote the power difference between both spectra, the dashed black line a smoothed mean obtained using local polynomial regression fitting. *Right:* Same spectrum with a resolution bandwidth of 500 Hz and the curves *not* normalized.

To measure the noise levels, a similar setup as described in section 3.3.1 was employed, with the board being powered from a benchtop power supply, the PCB being set up for unity gain using its offset potentiometer (with the control input terminated), and a AGILENT *FieldFox N9912A* device being used as spectrum analyzer. To generate the RF signal, a TTI *TGR1040* adjustable RF source was used. The DIRE PCB was situated on a desk without any extra RF shielding, but no other RF (power) equipment was nearby when the measurement was performed.

Figure 3.4 shows the power spectra obtained directly after the RF source and after passing the signal through the DIRE board, with the RF source being set to generate 0 dBm at 100 MHz, with the carrier frequency subtracted from the horizontal axis for convenience. As discussed in the previous section, the DIRE board causes a constant attenuation of slightly above 6 dB. Thus, both signals were normalized so that the maximum (at 100 MHz) corresponds to 0 dBm for easier comparison.

It is easy to see visually that adding the multiplier PCB into the signal chain does not significantly increase the power in the sidebands up to 1 MHz above and below the carrier frequency beyond what is produced by the RF source. Due to this small difference, it is hard to extract meaningful data about the added noise levels, as the calculation is very sensitive to small imperfections in the measurement setup. This fact is represented in figure 3.4 by the high variance in the position of the black dots, which represent the difference in power between the two measured spectra. As can be seen from the smoothed line, the results suggest a worst-case addition to the amount of carrier amplitude noise of -70 dB, and a white noise floor of about -100 dBm/10 Hz.

The first figure seems to imply that the DIRE PCB causes a small, but noticeable increase in the noise floor. However, this is only an artefact produced by normalizing the measurement results combined with the finite dynamic range of the spectrum analyzer. In the second graph, where the spectra have not been normalized, the noise floor is the same between the two measurements. The peaks in the spectrum of the RF source are now masked by the noise floor because of the negative

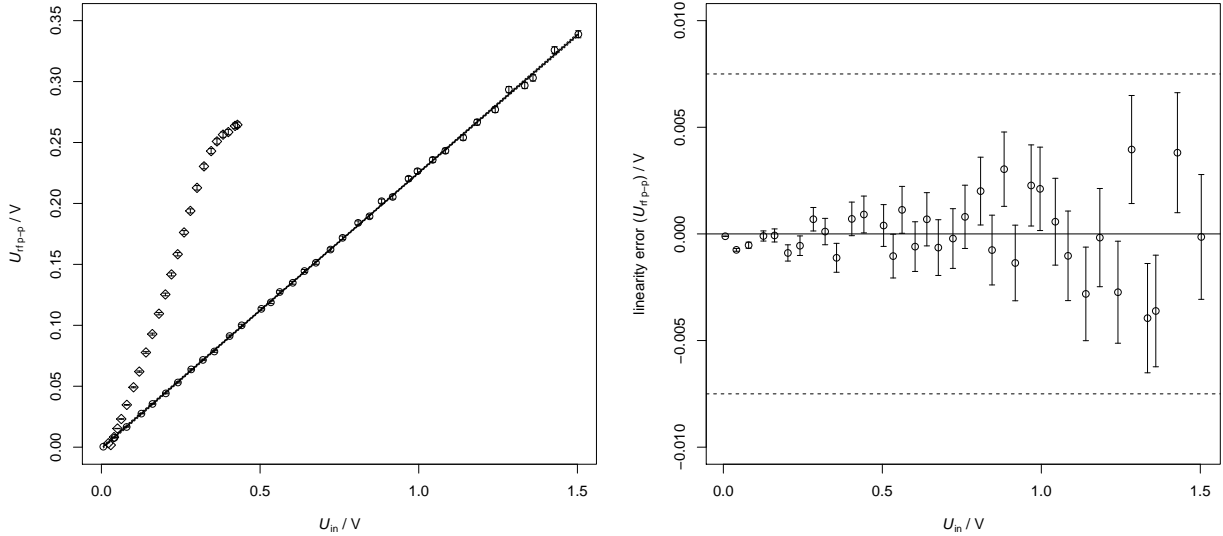


Figure 3.5.: Control input linearity measurements. In the left plot, circles show the measurements for the DIRE PCB, diamonds the results for a MINI-CIRCUITS diode ring mixer as a comparison base. The solid line shows a linear regression to the DIRE data. The right plot shows the residuals of this fit, i.e. the linearity error, with the dashed lines marking the typical error range as per the datasheet of the used multiplier IC.

gain of the DIRE board.³

In addition to that, measurements of the spectra with a larger frequency span were performed. No additional harmonics or spurious peaks beyond those produced by the RF source were found up to 500 MHz.

3.3.3. Control Input Linearity

As mentioned in the above, a secondary design goal was to offer not only a reasonably large control voltage range (≥ 1 V), but also to try to achieve a linear relation between the RF output and control input amplitudes. While a reasonably smooth response could e.g. be corrected for by using a lookup table in the pulse shaping controller, a linear response simplifies the design of these components.

The linearity error on the AD835 is specified as 0.3 % FS typ., 0.5 % FS max. in its datasheet, however only for low frequencies⁴. To actually measure the performance with RF applied, a similar setup as described in section 3.3.2 was used, with the RF carrier power, measured using the AGILENT *FieldFox N9912A* spectrum analyzer with a resolution bandwidth of 100 Hz, considered as a function of the control voltage, as measured using a UNI-T *UT61D* multimeter.

For the Mini-Circuits mixer, an ATLANTEC RF *ANS2-0080-050* device was used to provide a tone at 100 MHz and 0 dBm. The control voltage was fed directly into the mixer from an adjustable constant voltage supply. From 0 V to the point where the maximum allowable IF current was reached, the voltage was increased in a number of steps and the associated RF powers recorded.

For the measurements on the DIRE PCB a TTI *TGR1040* bench-top RF source was employed to generate a signal at 100 MHz and -3 dBm, with the control voltage again set using the on-board offset potentiometer, the input being terminated. The measurement was stopped at 1.5 V, which

³The noise floor in the second spectrum is higher overall because of the coarser resolution bandwidth.

⁴From the data sheet wording, it is unclear whether the “low-frequency” restriction applies only to the considered input or also to the other factor. Also, it is not clear whether the “full scale” qualifier applies to the output with the input ports at nominal full-scale values (1 V), or the max. output voltage swing of 2.5 V typ.

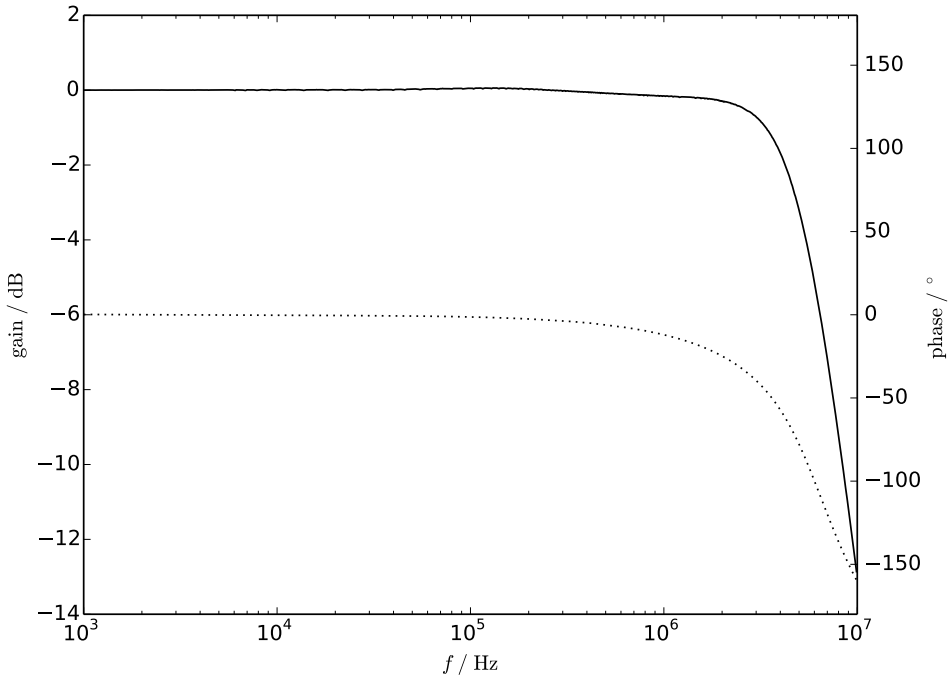


Figure 3.6.: Frequency response of the DIRE control input, measured by biasing the RF input to 1 V DC after the coupling capacitor (1000 points from 1 kHz to 10 MHz). The solid line is the gain as a function of frequency (normalized to 0 dB at DC), the dotted line the associated phase.

is already above the typical clipping level quoted in the AD835 data sheet. In lab usage, however, several devices were found to handle voltages as high as 3 V without irreversibly taking damage, with the hard clipping limit varying around 1.6 V.

This measurement procedure is unfortunately not very accurate, as the logarithmic amplifier in the spectrum analyzer leads to a large effect of noise on the voltage levels for higher power levels. Additionally, the spectrum analyzer was not configured for averaging over multiple sweeps. Based on the observations while measuring, this statistical error was estimated as 0.15 dBm (the absolute magnitude error of the spectrum analyzer is specified even higher at 0.4 dBm. The growing effect on the uncertainty of the RF voltage amplitude is immediately visible in the error bars of the results shown in figure 3.5).

Nevertheless, the measurement allows comparing the general linearity properties between the MINI-CIRCUITS mixer and the DIRE PCB. While for the former, a positive curvature is visible in the amplitude plot in the “linear” region before the roll-off, no non-linear trend is visible in the fit residual plot for the DIRE PCB even beyond its nominal input range of 1 V. Even considering the large uncertainties, the measurement results are clearly within the specified typical linearity error limit for the AD835 IC, 0.3 % FS.

3.3.4. Control Input Transfer Function

Although the RF performance of the two input channels of the AD835 chip differs slightly, their frequency response is largely comparable. This means that the raw -3 dB bandwidth on the control channel is comparable to the specified 250 MHz as well, and so the frequency response of the DIRE control input should be completely dominated by the second-order RLC lowpass at its input.

To verify this, the DIGILENT *Analog Discovery Kit* was used to measure the control input transfer function. It offers two ADC input channels and a DAC output channel controlled by an FPGA.

Using the vendor-provided *Waveforms* software, it can be used as an USB oscilloscope, arbitrary waveform generator, logic analyzer, and also as a vector network analyzer with a range of 10 MHz.

For the measurement, two SMA adapter cables were fashioned to accomodate the pin header connections for the *Analog Discovery Kit* waveform generator, phase reference, measurement and ground connections. No attempts to properly match the input and outputs to 50Ω characteristic impedance were made due to the relatively low frequencies involved. To avoid needing to drive the carrier input of the DIRE board with RF, which would have required an RF detector at its output, a makeshift needle probe was used to apply a constant DC voltage of 1 V behind the RF input coupling capacitor.

For further analysis, the bespoke ZIP/XML *Waveforms* network analyzer save file format was reverse-engineered and a small program written to export the transfer function data in a standard text format. The resulting transfer function for the DIRE board with the 1 MHz low pass filter is depicted in figure 3.6.

3.3.5. RF Feedthrough and Output Offset

To evaluate the feedthrough performance, an RF signal of 4 dBm at 100 MHz was applied to the DIRE board, and the control input held at a constant 0 V (an EVIL controller was connected, although a simple terminator could have been used). With the power to the DIRE PCB turned off⁵, a power of -74 dBm was measured at the output, giving a best-case baseline of -78 dB.

The DC supply was then turned on and the offset potentiometer tuned so as to minimize the power reading on the spectrum analyzer. The best result that could be reached is -66 dBm, which corresponds to a minimum feedthrough gain of -70 dB.

Since the output of the DIRE board is DC-coupled, the downstream device(s) must be able to cope with a small constant offset generated by the multiplier chip. The AD835 IC is specified for an offset voltage of ± 25 mV typ., ± 75 mV max., and similar figures were indeed observed when testing the board. This is not likely to be a problem for typical applications, as most equipment that would be used after the DIRE board, such as typical RF amplifiers, features AC-coupled inputs.

⁵This is reasonably safe to do with the DIRE board due to the topology of the AD835 chip and the external termination resistor. In general, signals should not be applied to unpowered RF equipment.

4. FPGA-based PID Controller

The laser intensity stabilization and pulse shaping scheme discussed in this report involves adjusting the control input of the RF multiplier used for feeding the AOM according to the light intensity signal measured by a photodiode. For this task, the *EVIL* controller hardware platform was used. It had previously been developed in the group for general stabilization and locking tasks, such as frequency-stabilizing lasers using a reference cavity or locking of cavities to the laser source. As it is centered around a field-programmable gate array (FPGA) chip, the controller functionality can be easily adapted to different systems.

In this chapter, first the necessary basics in control theory are reviewed, followed by a discussion of the widely known and used proportional-integral-(filtered-)derivative (PIDF) controlling scheme. Its discrete-time representation is derived and the conceptual hardware realization is discussed. After that, a controlling algorithm for time-delay dominated systems (*Smith prediction*) is presented, along with a discussion of the intricacies of adapting this scheme for AOM-based laser pulse shaping. Simple numerical simulations of the loop performance are presented, and finally an overview of the EVIL controller as modified for use in pulse shaping applications is presented.

4.1. Control Theory Fundamentals

Consider a general system G with a single real input quantity $x(t)$ and a single output $y(t)$. A fundamental concept is that of representing real functions in the *Laplace-* or *s-space* by taking their *Laplace transform*. The Laplace transform $\mathcal{L}[f(t)]$ is given as

$$\mathcal{L}[f(t)](s) := \int_0^{\infty} f(t)e^{-st}dt. \quad (4.1)$$

If this integral converges, the Laplace transform of $f(t)$ is said to exist. In control theory, by convention a lower-case letter designates a time-domain function $f(t)$, whereas an upper-case letter represents the corresponding Laplace-transformed function $F(s) := \mathcal{L}[f(t)](s)$.

The behavior of the output of the system G in response to its input is expressed in the Laplace domain by its *transfer function* $G(s)$, which is simply

$$G(s) := \frac{Y(s)}{X(s)}. \quad (4.2)$$

From its definition in equation (4.2), it is immediately clear that the transfer function is multiplicative, in the sense that the action of two concatenated single-input-single-output (*SISO*) systems G_1 and G_2 is described by the compound transfer function $G(s) = G_2(s)G_1(s)$.

Due to linearity of the Riemann integral, equation (4.1) implies that the Laplace transform is linear, $\mathcal{L}[\alpha x(t) + y(t)](s) = \alpha X(s) + Y(s)$. In control theory, a commonly used convention is to set the time-domain functions to zero for $t \leq 0$ and additionally for small positive t values as required to make boundary terms vanish in integral transformations. Using this convention, a time delay $f(t) \mapsto f(t - \tau)$ corresponds to a multiplication by an exponential $F(s) \mapsto e^{-s\tau}F(s)$ in the Laplace domain.



Figure 4.1.: General feedback loop consisting of a controller $C(s)$ and the system $G(s)$.

Another characteristic of the Laplace transform that makes it well-suited for control theory applications is that it reduces derivation and integration to simple algebraic expressions: Under the aforementioned boundary conditions, definition (4.1) immediately implies that

$$f(t) \mapsto \frac{df}{dt}(t)$$

corresponds to a simple multiplication

$$F(s) \mapsto sF(s),$$

whereas integration

$$f(t) \mapsto \int_0^t f(t') dt'$$

is represented by the transformation

$$F(s) \mapsto \frac{1}{s}F(s).$$

4.1.1. Feedback Control

In general, the goal of a control loop is to bring the output $Y(s)$ of a given system in agreement with a given *set point* $R(s)$ by adjusting its input $X(s)$. If the transfer function $G(s)$ of the system is perfectly known, this could theoretically be achieved by simply applying its inverse to the set point, $X(s) = G(s)^{-1}R(s)$.¹

However, in practice the transfer function is hardly ever known exactly, for example due to nonlinearities in the system. Additionally, there often are external disturbances, such as the laser noise in the case of this thesis, the behavior of which is not known in advance. The most straightforward way to accommodate this is by including a *feedback path* in the control scheme.

The general form of simple feedback control loops is shown in figure 4.1. The output $Y(s)$ of the system is detected by some kind of sensor (a photodiode at a pick-off in the beam path in this case), and subtracted from the set point $R(s)$ to form the *error signal*

$$E(s) = R(s) - Y(s). \quad (4.3)$$

For simplicity, this detection is assumed to be free from imperfections here. The error signal is then processed by a *controller* that is described by a transfer function $C(s)$, the output of which is the input to the system, $X(s)$.

By combining the identities

$$Y(s) = G(s)X(s) = G(s)C(s)E(s) \quad (4.4)$$

and

$$E(s) = R(s) - Y(s), \quad (4.5)$$

¹At least as long as the controlled system is stable. Otherwise, the unavoidable small imperfections in the realization would lead to chaotic behavior.

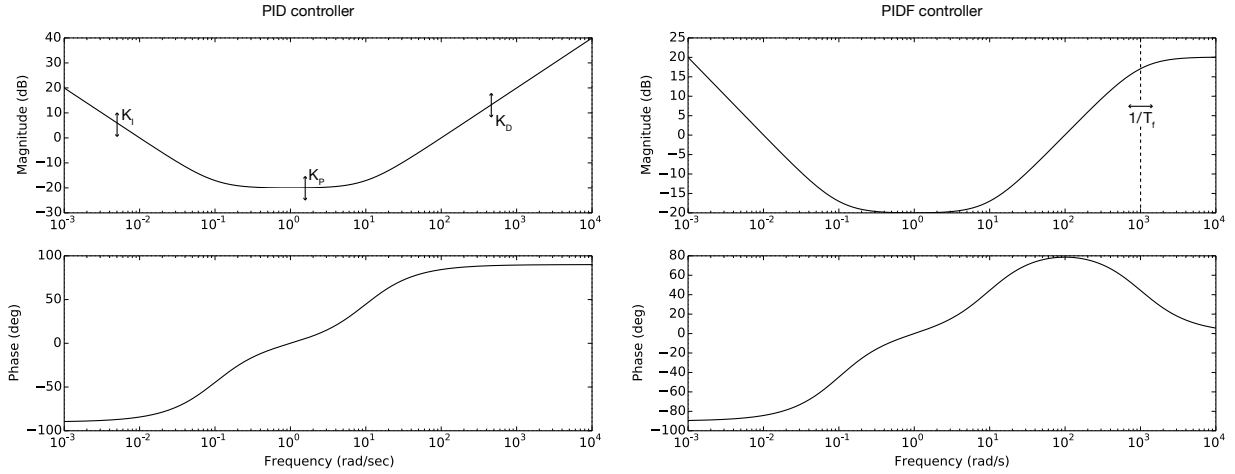


Figure 4.2.: *Left:* Bodé plot of a PID controller with transfer function $C(s) = 0.1 + \frac{0.01}{s} + 0.01 s$. *Right:* Same controller with a low-pass filter added to the derivative branch, $C(s) = 0.1 + \frac{0.01}{s} + \frac{0.01 s}{1+0.001 s}$.

it follows immediately that the transfer function of the total system, i.e. the response $Y(s)$ in relation to the set point $R(s)$, can be written as

$$\frac{Y(s)}{R(s)} = \frac{C(s)G(s)}{1 + C(s)G(s)}. \quad (4.6)$$

The product $C(s)G(s)$ is usually referred to as the *open loop transfer function* $O(s)$. Note that per equation (4.6), the control loop is unstable if there is a point where $O(s) + 1 = 0$, i.e. we have for the magnitude $|O(s)| = 1 = 0$ dB, $\arg O(s) = \pi = \pm 180^\circ$. This motivates the definition of two quantities related to the stability of a control loop, the *gain margin* g and the *phase margin* ϕ :

Let s_π be a point where $\arg O(s_\pi) = \pi$. Then,

$$g := \frac{1}{|O(s_\pi)|}, \quad (4.7)$$

and is usually expressed on a logarithmic scale in dB (if more than one such point exists, than the minimum of all is taken). That is, the gain margin is the amount of overall gain that could be added to the system before it goes unstable.

Conversely, let s_0 be a point where $|O(s_0)| = 1$. Then,

$$\phi := \pi + \arg O(s_0), \quad (4.8)$$

where again the smallest value is taken if more than one such point s_0 exists. The phase margin thus describes the amount of phase lag that could be added to the system before it goes unstable. For brevity of notation, we assume here that the nearest point where the system goes unstable corresponds to a phase of $-\pi$, not π , (i.e. a phase lag). This is often the case in physical systems due to causality, and particularly in those discussed in this report.

4.1.2. PID(F) Control

Generally, the aim of a controller is to track the reference signal as closely as possible. In doing so, a system should both keep transients stemming from external disturbances low in magnitude and short-lived, and reach an error signal of zero in the steady-state. The optimal choice of $C(s)$ depends on the system $G(s)$ and the nature of the external disturbances.

However, there is a controlling scheme which is universal enough to yield reasonable results on many commonly encountered systems, while still allowing for an intuitive understanding of the tuning parameters, *proportional-integral-derivative (PID)* control. It is in widespread use in many different control applications, and combines the control action from three parts,

$$x(t) = x_P(t) + x_I(t) + x_D(t). \quad (4.9)$$

The first part, $x_P(t)$, is called the *proportional* term, and is simply proportional to the error signal,

$$x_P(t) = K_P e(t). \quad (4.10)$$

The second part, $x_I(t)$, is proportional to the *integral* of the error signal,

$$x_I(t) = K_I \int_0^t e(t') dt', \quad (4.11)$$

and the third part, $x_D(t)$, is proportional to the *derivative* of the error signal:

$$x_D(t) = K_D \frac{de(t)}{dt}. \quad (4.12)$$

Using the transformations discussed in the previous sections, the total transfer function $C(s)$ for a PID controller can thus be written as

$$C_{\text{PID}}(s) = K_P + K_I \frac{1}{s} + K_D s. \quad (4.13)$$

The general Bodé plot of $C_{\text{PID}}(s)$ is shown in figure 4.2. Note that the integral term mainly affects the lower frequencies and generates a phase lag in this region, whereas the proportional term manifests itself as a frequency-independent and phase-neutral gain stage. The derivative term generates gain associated with a phase lead and increases in strength the higher the signal frequencies are.

This last fact makes use of derivative control often difficult in physical systems, as it can lead to large amplification of high-frequency noise components in the feedback signal that might even be at higher frequencies than the achievable control bandwidth anyway. A natural extension of PID control thus is to add an adjustable low-pass filter to the derivative term. The transfer function for a low-pass filter with time constant T_f is

$$\frac{1}{1 + T_f s},$$

so the total transfer function of a *proportional-integral-filtered-derivative (PIDF)* controller becomes

$$C_{\text{PIDF}}(s) = K_P + K_I \frac{1}{s} + K_D \frac{s}{1 + T_f s}. \quad (4.14)$$

As can be seen in figure 4.2, The added term results in a gain roll-off towards higher frequencies.

4.1.3. Discrete Time Representation

So far, the discussion was based on a continuous time variable t and the associated continuous quantity in the Laplace domain, s . However, the controller is to be implemented on a digital FPGA chip, which invariably entails operation in discrete time steps (samples). To describe the action of controllers in this environment, a useful tool is the *z-transform*, which interprets the measured

values as coefficients in a formal power series. For samples $f[n]$ of a function f taken at equidistant points in time, the (unilateral) z -transform is defined as

$$\mathcal{Z}[f[n]](z) := \sum_{n=0}^{\infty} f[n]z^{-n}, \quad (4.15)$$

where z is a complex parameter.

This mapping is trivially linear, and similar to the Laplace transform, functions in the z -domain are usually denoted by an upper-case letter: $F(z) = \mathcal{Z}[f[t]](z)$. Formally, we have

$$z^{-1}F(z) = z^{-1}\mathcal{Z}[f[n]](z) = \sum_{n=0}^{\infty} f[n]z^{-(n+1)} = \sum_{n=1}^{\infty} f[n-1]z^{-n} = \mathcal{Z}[f[n-1]](z) - f[-1],$$

or if $f[t] = 0 \quad \forall t < 0$, as usually chosen in control theory (see last section)

$$z^{-1}\mathcal{Z}[f[n]](z) = \mathcal{Z}[f[n-1]](z). \quad (4.16)$$

Comparing equation (4.16) to the time shift property for the Laplace transform discussed in section 4.1 suggests the following identification:

$$z^{-1} = e^{-sT_S}, \quad (4.17)$$

where T_S is the sampling timestep. Taylor approximation yields a rational expression

$$z^{-1} = \frac{e^{-\frac{sT_S}{2}}}{e^{\frac{sT_S}{2}}} \approx \frac{1 - \frac{sT_S}{2}}{1 + \frac{sT_S}{2}}, \quad (4.18)$$

or

$$s \approx \frac{2}{T_S} \frac{1 - z^{-1}}{1 + z^{-1}}. \quad (4.19)$$

By substituting z for s in the Laplace-domain expression for a continuous-time transfer function as indicated by equation (4.19), we can obtain its discrete-time equivalent. This is referred to as the *bilinear transform*.

Now, let $G(z) = \frac{Y(z)}{X(z)}$ be a discrete-time transfer function of the form

$$G(z) = \frac{a_0 + a_1 z^{-1} + a_2 z^{-2} + \dots}{1 - b_1 z^{-1} - b_2 z^{-2} - \dots} = \frac{\sum_{k=0}^N a_k z^{-k}}{1 - \sum_{l=1}^M b_l z^{-l}}. \quad (4.20)$$

Applying the linearity of the z -transform and property (4.16) yields

$$\mathcal{Z}\left[\sum_{k=0}^N a_k x[n-k]\right] = \mathcal{Z}\left[y[n] - \sum_{l=1}^M b_l y[n-l]\right]. \quad (4.21)$$

or by applying the inverse z transform,

$$y[n] = \sum_{k=0}^N a_k x[n-k] + \sum_{l=1}^M b_l y[n-l]. \quad (4.22)$$

The significance of equation (4.22) lies in the fact that if G is a filter or controller that is to be implemented digitally, it provides an explicit recurrence relation for the output value $y[n]$ based on the input values $\{x[n], \dots, x[n-N]\}$ and the previous output values $\{y[n-1], \dots, y[n-M]\}$.

Applying all the above steps to the transfer function for the PIDF controller $C_{\text{PIDF}}(s)$ given in equation (4.14) yields

$$C_{\text{PIDF}}(z) = \frac{a_0 + a_1 z^{-1} + a_2 z^{-2}}{1 - b_1 z^{-1} - b_2 z^{-2}}, \quad (4.23)$$

i.e. the recurrence relation

$$y[n] = a_0 x[n] + a_1 x[n-1] + a_2 x[n-2] + b_1 y[n-1] + b_2 y[n-2] \quad (4.24)$$

with the *feed-forward coefficients*

$$a_0 = K_P + K_I T_h + \frac{K_D}{T_f + T_h} \quad (4.25)$$

$$a_1 = 2 \frac{-K_D + K_P T_f + K_I T_h^2}{T_f + T_h} \quad (4.26)$$

$$a_2 = \frac{K_D - (T_h - T_f)(K_P - K_I T_h)}{T_f + T_h} \quad (4.27)$$

and the *feed-back coefficients*

$$b_1 = 2 \frac{T_f}{T_f + T_h} \quad (4.28)$$

$$b_2 = 1 - 2 \frac{T_f}{T_f + T_h}, \quad (4.29)$$

where $T_h = T_S/2$ is half the sampling interval of the controller.

4.2. Modelling the AOM Input Power to Laser Intensity Relation

In order to design a controller for the intensity stabilization control loop, it would be desirable to have a good model of the system behavior in the form of a transfer function. Considering the setup to be a SISO system, the input would be the control voltage to the DIRE RF modulator board $v_{ctrl}(t)$, and the output would be the intensity of the laser beam after the AOM, $i_{out}(t)$. The control loop is closed by a photodiode at a pick-off in the output beam. Devices with good linearity and rise time specifications were available, so the voltage at the controller input could be considered to mirror the actual laser intensity in good approximation.² As shown by the measurement results in chapter 3, the DIRE RF multiplier can also be considered ideal in good approximation if the corner frequency of the control input filter is chosen high enough. Thus, the focus in the following is on the behavior of the AOM.

Let $r(t)$ be the diffraction efficiency of the AOM. In section 2.2, the two main features in the dynamic behavior the AOMs were outlined: First, the time delay due to the distance of the sound emitters to the beam path, and second, the finite rise time caused mainly by the non-zero waist of the laser beam. From these considerations, we have the model

$$\frac{R(s)}{V_{ctrl}(s)} = L(s) e^{-s\tau}, \quad (4.30)$$

where τ is the latency and $L(s)$ is some low-pass filter (e.g. a simple first order filter, $L(s) = (1+s T)^{-1}$ for a time constant T).

²In the numerical simulations described in section 4.4, a small detection noise term was included additionally.

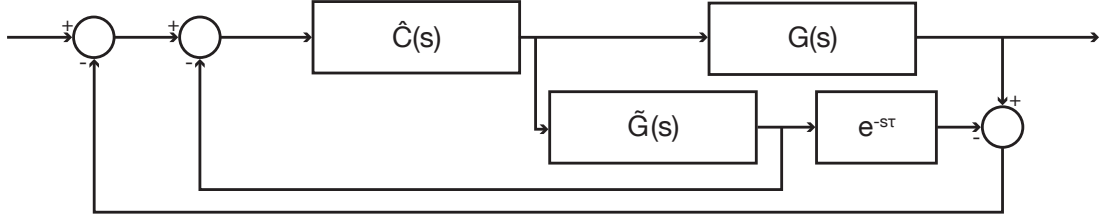


Figure 4.3.: Block diagram of a Smith predictor with inner controller \hat{C} , system model \tilde{G} and delay time τ .

For the (low) laser powers used in the experiments, the AOM medium behaves linearly in good approximation, $i_{out}(t) \propto i_{in}(t)$. Furthermore, for a double pass AOM setup, $i_{out}(t)$ is not proportional to the diffraction efficiency, but to its square $r(t)^2$:

$$i_{out}(t) = r(t)^2 i_{in}(t). \quad (4.31)$$

Thus, even for a constant $i_{in}(t)$, the relation of $i_{out}(t)$ to $v_{ctrl}(t)$ is non-linear, and cannot easily be expressed in terms of a Laplace-space transfer function (the fraction $I_{out}(s)/V_{ctrl}(s)$ would depend on $V_{ctrl}(s)$).

However, the most important application of the model in the scope of this project was in addressing the fact that the simple PI controlling scheme described in the above yielded only very mediocre setpoint tracking performance for the control loop setup in our laboratory. Investigations showed (see appendix A for details) that for the AOMs used in the lab setup, the dominant effect on control loop performance comes from the AOM response latency τ . The transfer function for a pure time delay is $e^{-s\tau}$, i.e. it causes a phase lag growing linearly with the frequency ω , $\phi(\omega) = \arg(e^{-i\omega\tau}) = -\omega\tau$. Because the transfer function is an exponential, it cannot be well compensated by a simple controller described by a rational transfer function. The controller for the composite transfer function $\hat{G}(s)e^{-s\tau}$ is thus forced to operate with much lower gains than would be desirable for the non-delayed system $\hat{G}(s)$ to guarantee a sufficiently large gain margin.

Thus, modelling the time delay correctly was more important than the details of the high-frequency roll-off behavior. Furthermore, for feedback-less pulse shaping applications, a square root output mapping module was implemented for the digital controller (see section 4.5), such that $v_{ctrl}(t) \propto \sqrt{x(t)}$, where $x(t)$ is the controlled variable. This cancels the square term such that in the steady state (!), $i_{out}(t) \propto x(t) i_{in}(t)$. Thus, if $i_{in}(t) = i_{in} = \text{const.}$, the system behavior can be approximated as

$$\frac{I_{out}(s)}{X(s)} = \alpha i_{in} \tilde{L}(s) e^{-s\tau}, \quad (4.32)$$

where α is a proportionality constant and $\tilde{L}(s)$ models the AOM rise time. $\tilde{L}(s)$ would be chosen such as to yield an acceptable representation of the dynamics of a given AOM model. In the numerical experiments performed as part of this project, a simple first-order lowpass filter with time constant determined from the AOM step response was used.

4.3. Smith Predictors

Intuitively, one might suspect that for time delay dominated systems, a control scheme that explicitly takes this delay into consideration in addition to linear control theory could lead to better results. One such augmented system is *Smith prediction*. It is based on the assumption that the ideal response for a time delayed system $G(s) = \hat{G}(s)e^{-s\tau}$ is the same that a given controller $\hat{C}(s)$ gives for the non-delayed system $\hat{G}(s)$, only delayed in time by τ . In terms of the closed-loop transfer

functions, this requirement can be expressed as

$$\frac{C(s)G(s)}{1 + C(s)G(s)} = \frac{C(s)\hat{G}(s)}{1 + C(s)\hat{G}(s)e^{-s\tau}}e^{-s\tau} \stackrel{!}{=} \frac{\hat{C}(s)\hat{G}(s)}{1 + \hat{C}(s)\hat{G}(s)}e^{-s\tau}. \quad (4.33)$$

Solving (4.33) for the controller $C(s)$ yields

$$C(s) = \frac{\hat{C}(s)}{1 + \hat{C}(s)(1 - e^{-s\tau})\tilde{G}(s)}, \quad (4.34)$$

where $\tilde{G}(s)$ is an approximation for the real non-delayed system $\hat{G}(s)$ in the controller. This expression has a straightforward interpretation in terms of an inner and an outer feedback loop, as shown in figure 4.3. Immediately after the controller output, the system response is predicted and fed back to the controller input, forming the inner loop. Additionally, the model output is fed into a time-delay element, the output of which is subtracted from the actual system output to form the outer loop. [17]

If the model for the system is perfect, i.e. $\tilde{G}(s) = \hat{G}(s)$, the contributions to the outer feedback path cancel exactly, and the whole system reduces to the non-time-delayed case with a single time delay at the output, just as desired. In real systems, this will never exactly be the case. Here, the outer feedback feedback loop provides compensation, if of course with a time delay of τ . The better the model \tilde{G} , the smaller this contribution will be, and the closer the gains of \hat{C} can thus be to the optimal choice for the non-delayed system without rendering the loop unstable.

For the laser intensity control loop, the model for G would be based on equation (4.32). There is one additional complication, however: The laser input intensity i_{in} , which is a multiplicative factor in the model, is not a constant, but in fact the source of the disturbance that the controller is meant to reduce. Thus, for the model to be accurate, the laser intensity model has to be updated while the controller is running. An estimate for the laser intensity can be simply gained by dividing the measured photodiode signal by the model for the current diffraction efficiency. The model would usefully be updated through a low-pass filter to avoid introducing excess amounts of noise. However, the model updating introduces another (time-delayed) feedback path, and can thus be an additional source of oscillations.

4.4. Simulation Results

To evaluate the setpoint tracking and disturbance rejection capabilities of different candidate control schemes for the intensity stabilization loop, a basic discrete-time numeric simulation of the system was written using NumPy. This approach was chosen in addition to a purely analytical Laplace-domain based approach to be able to benchmark the algorithms exactly as they would be implemented on the FPGA chip of the EVIL controller. The simulations were performed after having already determined experimentally that a simple PI controller does not offer satisfactory set point tracking performance. The primary goal thus was to evaluate whether adding a filtered-derivative term or implementing Smith prediction would potentially lead to improved results.

In the simulation, the action of the AOM was simulated as a first-order low-pass filter with time constant $T = 0.4 \mu s$ cascaded with a time delay of $\tau = 1.4 \mu s$. The sampling/update rate was 96 MHz, as it would be on the EVIL platform. For the Smith predictor, the same model as used for simulating the AOM action was assumed, with only a slight mismatch in the parameters of 1 % of the respective values. The laser intensity model was updated via a low-pass filter with time-constant 500 μs . Two types of scenarios were simulated:

The first consisted of an evaluation of the noise rejection performance. For this, the input laser intensity was assumed to carry white noise with a peak amplitude of 0.05 times the mean intensity.

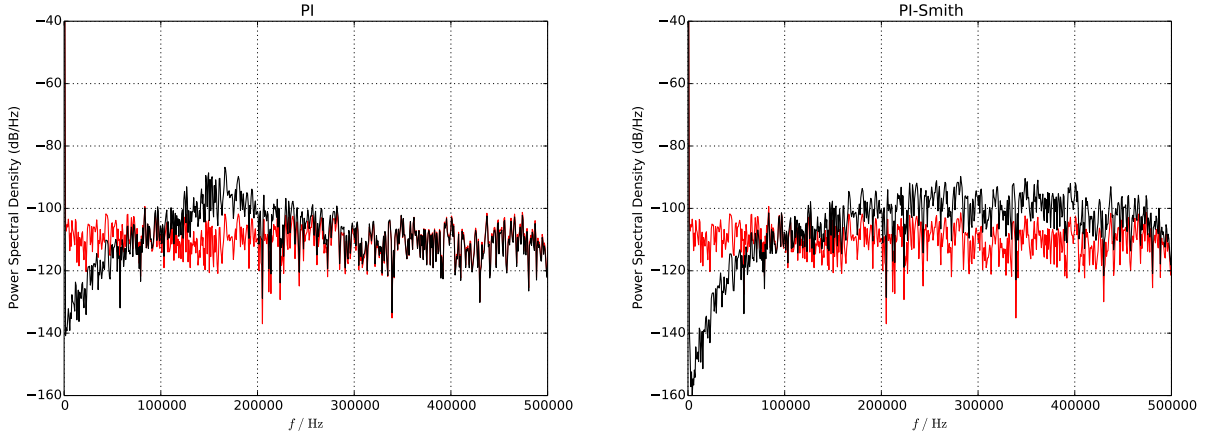


Figure 4.4.: Noise rejection simulation results for a simple PI controller and a Smith predictor based on a PI controller. The power spectral density of the noise on the input (laser intensity) is shown in red, the spectrum of the controlled output (after the AOM) in black.

The controller action for this case, including a small (0.1 %) white noise component in the detection circuitry, was then simulated, and the resulting output noise spectrum computed by taking the Fourier transform of the simulated intensity at the AOM output.

Figure 4.4 shows the results for a simple PI controller and a Smith predictor, again with a simple PI controller as the inner controller \hat{C} . For both controllers, the gains were adjusted for maximum noise rejection bandwidth in stable operation. In fact, the gains for the simple PI controller were probably higher than they would be taken in typical operation, as evidenced by the large “servo bump” already appearing at 150 kHz.

The larger gains enabled by the time delay compensation in the Smith predictor case lead to a significantly better noise rejection in the very low frequencies. The behavior around the rejection bandwidth limit near 100 kHz does not improve significantly, however. Thus, it would be questionable whether the benefits of the Smith predictor would be worth the significantly increased complexity in implementation and the required calibration based on this alone, especially since it is also predicted to exhibit a wide-band increase in noise towards higher frequencies.

The second simulation concerned the setpoint tracking performance of the controller. In this case, the real laser noise profile was approximated as a combination of $1/f$ and white noise, generated by taking the Fourier transform of white noise and shaping the coefficients by the function

$$n(\omega) = \begin{cases} \left(\frac{\omega_0}{\omega}\right)^\alpha & \text{for } \omega \leq \omega_0 \\ 1 & \text{else} \end{cases},$$

where $\omega_0 = 1$ MHz, $\alpha = 1.3$.

Again, the gains for both controllers were tune for best performance, here characterized by good setpoint tracking while minimizing overshoot. The results for a square pulse of 5 μ s duration are shown in figure 4.5. As the loop delay of 1.3 μ s is significant compared to the duration, the PI controller heavily distorts the signal shape – for the chosen gains, once the overshoot has settled, the end of the pulse is already reached. At the same time, the low integrator gain is still limiting the rise time of the signal. In contrast to that, the Smith predictor-based controller is able to follow the set point much more closely, with the higher gains also enabling shorter rise times.

The laser intensity model updating positively effected the noise rejection simulation results and also led to slight improvements in the pulse tracking response for noise with a high amount of low-frequency content, as expected. However, the updating also caused a noticeable increase in ringing effects in the step response of the system. The chosen low-pass time constant of 500 μ s reduced this

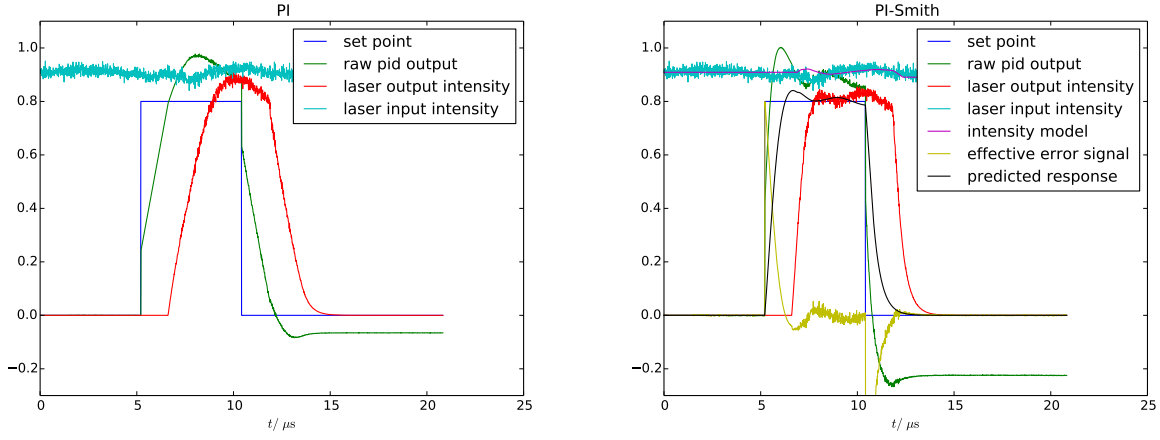


Figure 4.5.: Set point performance simulation for a simple PI controller and a Smith predictor based on a PI controller. The target function, a square pulse of 5 μs duration is shown in dark blue, the effective laser intensity at the loop input in light blue. The raw controller output is shown in green, and the effective resulting pulse (consisting of the controller output clipped to [0, 1], low-pass filtered, time-delayed and multiplied by the laser input intensity) in red. For the Smith predictor, additionally shown are the inferred intensity model used in the model branch of the controller, the predicted AOM response, and the effective error signal at the inner PI controller resulting from that.

phenomenon to negligible amounts, but there might be a better way of modelling the system to avoid this altogether.

As mentioned above, the main goal of the simulation was to provide an indication whether different more complex control schemes might be worth investigating, and to provide a platform to experiment with different implementations. Thus, the prediction model chosen was almost certainly better than realistically be achieved for a real AOM. Further simulations showed, however, that Smith prediction yields considerable set point tracking improvements even for discrepancies in the AOM low-pass time constant in the tens of percents as long as the loop delay time constant is estimated with good accuracy, which is relatively easy to accomplish experimentally.

Results for the PIDF controller are not presented here, since no significant improvement compared to the simple PI controller could be observed in the simulations. This might be in part be owed to the simple system used for modelling the AOM behavior in the simulation, though.

4.5. The EVIL Controller

The EVIL controller platform is a Eurocard-sized unit (6 HU), designed to offer a flexible basis for control and locking applications. Before the project was started, the system was in use as a simple one-channel PI controller for several locking applications. In this section, an overview of the adapted firmware for use in the pulse shaping control loop is presented.

An overview of the system is shown in 4.6. The main hardware elements are a XILINX *Spartan 3E*-series FPGA chip, which is connected to two 10 bit analog-to-digital converters (ADCs), a fast 14 bit and a serially controlled 10 bit digital-to-analog converter (DAC), an external TTL signal input and a serial computer interface (via USB). It is designed to slot into a 19" rack backplane for power.

The gain of the analog inputs is adjustable using a potentiometer in the gain section. In the pulse shaping firmware, one of the inputs captures the photo-diode response for control feedback. The other input can be used to supply an external setpoint voltage.

In most applications, however, the controller setpoint will be generated on the FPGA chip. For this, the basic sweeping support in the pre-existing EVIL firmware was extended in two ways: First, a simple DDS module allows generating square, sine and saw-tooth functions of adjustable frequency,

range, and offset. It is intended to be used while testing and adjusting the setup. Second, for actually generating the shaped laser pulses to be used in the experiment, a pre-existing spline interpolation core was adapted for the project and optimized to meet the timing requirements at the system clock frequency of 96 MHz.

The data for the spline core is stored in random-access memory embedded in the FPGA chip. Between the spline segment anchor points, cubic interpolation is performed using a recurrence relation in fixed-point arithmetic. Each waveform can consist of two separate parts which can be triggered individually using the external TTL input, as shown in figure 4.6: When the TTL trigger signal is pulled low, the first part of the waveform, usually the rising edge of the pulse, is played back. The output is then held at the last value until the input is asserted again and the second part of the waveform is generated. After the falling edge curve is completed, the system stands by for the next pulse. This design was chosen for ease of integration with the existing experimental control system, as it allows to re-use the same procedure for pulse area calibration as used when directly controlling the RF signal to the AOM with the TTL signal using an RF switch.

The scaled and shifted waveform generator signal can either be applied directly to the output stage for use in a simple pulse-shaping setup without feedback, or serve as the setpoint signal to the controller part of the core. Currently, only a simple PI controller is implemented. It has been slightly augmented over the basic EVIL design to offer better resilience against integrator overflow/underrun situations by extending the digital signal range beyond the available output range. If the controller output falls below zero or above full-scale, the output signal is clamped to the nominal range to allow the controller to recover from momentary overshoot.

To avoid integrator runaway in between laser pulses due to slight miscalibrations of the input offset (as e.g. caused by changing stray light levels on the in-loop photodiode), the controller can be automatically reset after a pulse has ended. The finite controller gains lead to an effective low-pass filtering and thus a small time lag of the pulse shape, so an adjustable time delay in the reset control path can be used to avoid prematurely cutting off the controller output.

The selected output signal (directly from the waveform generator/external input or the controller output) is then routed through an output conditioning section corresponding to the function

$$f(x) = a + b\sqrt{x} + c x, \quad (4.35)$$

where $a, b, c \in [0, 1]$ are adjustable parameters (and $[0, 1]$ is the full output range). The offset allows tweaking the logical zero level to match the RF multiplier input, and the scaling is used to fine-tune the RF signal level to match the used AOM model. As discussed in section 4.2, the square root mapping can be used to approximately linearize the intensity response in a double-pass AOM setup³, whereas in a single-pass setup, the linear term would be used. Only the fast DAC is actively used in the pulse shaping setup firmware to output the control signal.

The various parameters of the waveform generators, controllers and input/output stages can be tuned over the USB-serial interface. For this, the existing Python-based control software was adapted to allow access to the added settings. In addition, a continuously updated back-channel was added to warn the user if the input ADCs are overloaded or the PI controller hit an overflow condition. These error condition signals are extended in the FPGA hardware to make sure even small momentary overflow events are detectable by the user. A small separate program is used to upload spline data into the controller memory, which could be integrated into the main control interface in the future.

4.5.1. PIDF and Smith Predictor Implementation

Neither the filtered derivate controller nor a Smith prediction-based scheme could actually be implemented during the course of the project due to lack of time. However, it should definitely be

³The chosen square root implementation (semi-pipelined CORDIC) causes an extra latency of 9 cycles, or 94 ns, compared to the linear data path.

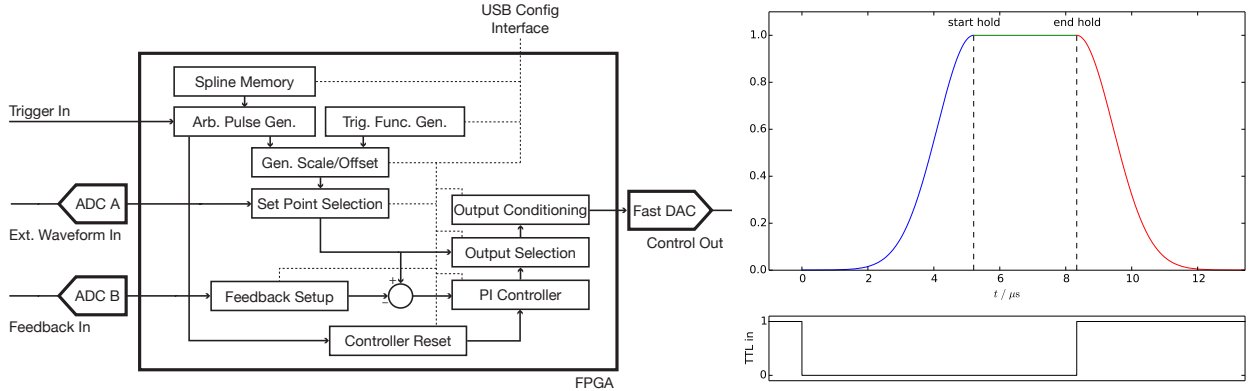


Figure 4.6.: Left: Block diagram describing the architecture of the EVIL pulse shaping firmware. **Right:** An example pulse with Gaussian edges, controlled by an external TTL trigger signal.

feasible to implement both schemes on the EVIL platform.

The recurrence relation for the PIDF controller, as given in equation (4.24), corresponds directly to the “biquad” second-order IIR filter primitive and is, in theory, suitable for implementation in an FPGA environment. The most timing-critical path is the multiplication $b_1 y[n - 1]$, the result of which is needed immediately the cycle after $y[n - 1]$ becomes available for the calculation of $y[n]$. However, for implementing this in a precision-constrained environment such as an FPGA, it might be advantageous to consider splitting the P/I/DF stages and implementing them in the straightforward way, summing them together at the end, to e.g. be able to use an integral accumulator register with a higher precision than otherwise possible due to timing constraints. This might lead to a slightly different discrete-time transfer function, but since (4.23) was obtained using bilinear approximation, it might not be necessarily inferior.

With regard to Smith predictors, the model could e.g. be implemented simply as two cascaded first-order low-pass filters, with the time constants being adjustable from the control software. The time delay would likely be best implemented as a ring buffer in the on-chip BRAM with a constant offset between the reading and writing addresses. The biggest challenge would be to offer a good way to adjust the model parameters to a given AOM setup. A workable scheme might be to provide a calibration mode where a step function is put out and the GUI software calculates the model response for the current parameters to display it alongside the actual system response as captured via the streaming function.

5. Results

After assembly and tests of the DIRE board were completed and the initial pulse shaping firmware was in a working state with a simple PI controller, several measurements of the performance of the complete control loop were made. The rather mediocre results were what prompted the investigations regarding more complex schemes, but unfortunately, Smith prediction and the other more complex schemes could not be implemented due to time constraints. Thus, the results should be regarded as a lower bound of what would be achievable with a more sophisticated setup.

5.1. Noise Rejection Bandwidth

One of the measurements was concerned with the noise rejection performance of the control loop. It was performed on the 854 nm beam path in the setup for the cryo and PCF traps, where similar experiments had coincidentally been performed as part of a different project at the same time. As the intensity noise levels on the laser beam were too low for an accurate measurement of the noise reduction, an AOM placed at the input to the setup was used to artificially induce intensity fluctuations on the beam. Following it, the setup consisted of a basic intensity stabilization loop as described in the previous chapters.

For initially modulating the beam, an INTRA-ACTION *ATD-2001A2* device was used. The RF was generated using the RF DDS system set to 167 MHz at -14 dBm, modulated using a DIRE board and amplified with two cascaded MINI-CIRCUITS *ZFL-1000VH2* and *ZHL-1-2W-S+* amplifiers. For the control loop, an INTRA-ACTION *AOM-802AF3* was used in single-pass configuration. It was driven using an 80 MHz signal generated by a TTI *TGR1040* RF source, also controlled by a DIRE board, and amplified directly using a MINI-CIRCUITS *ZHL-1-2W-S+* device.

In lieu of a proper wide-band noise source (which was not available at the time of the measurement), a simple function generator was used to generate a sinusoidal modulation of the noise AOM control voltage. The signal of the in-loop photodiode at the EVIL input was tapped off and monitored using an oscilloscope. For several excitation frequencies f_{sine} , the signal of the photodiode was then captured both with the controller engaged and with its output being held at a constant value. The difference in the maximum values of the power spectrum of the photodiode signal was then considered as the noise attenuation factor.

The results are shown in figure 5.1. For disturbance frequencies $f_{\text{sine}} < 1$ kHz, the plot shows a constant attenuation of around -46 dB. However, this is not (necessarily) the maximum noise rejection factor of the control loop, but merely the resolution limit of the oscilloscope used to capture the data: The bit width of the analog-to-digital converters in the front-end of the LECROY *WaveJet 324A* oscilloscope is 8 bit. This leads to an estimate for the best-case signal to noise ratio of $20 \log_{10}(2^{-8})$ dB = -48.2 dB. Further considering the fact that the signal was acquired in DC-coupled mode and the modulation amplitude was only approximately half that of the DC signal level, and thus the dynamic range of the oscilloscope inputs was not used optimally, this corresponds well to the measured maximum reduction. And indeed, inspecting the spectrum of the reveals that at lower frequencies, the signal peak at f_{sine} disappears into the noise floor once the controller is engaged.

Towards higher frequencies, the noise rejection ratio gain (on a logarithmic scale) deteriorates approximately linearly with the frequency (also on a logarithmic scale). At $f_{\text{sine}} = 20$ kHz, the

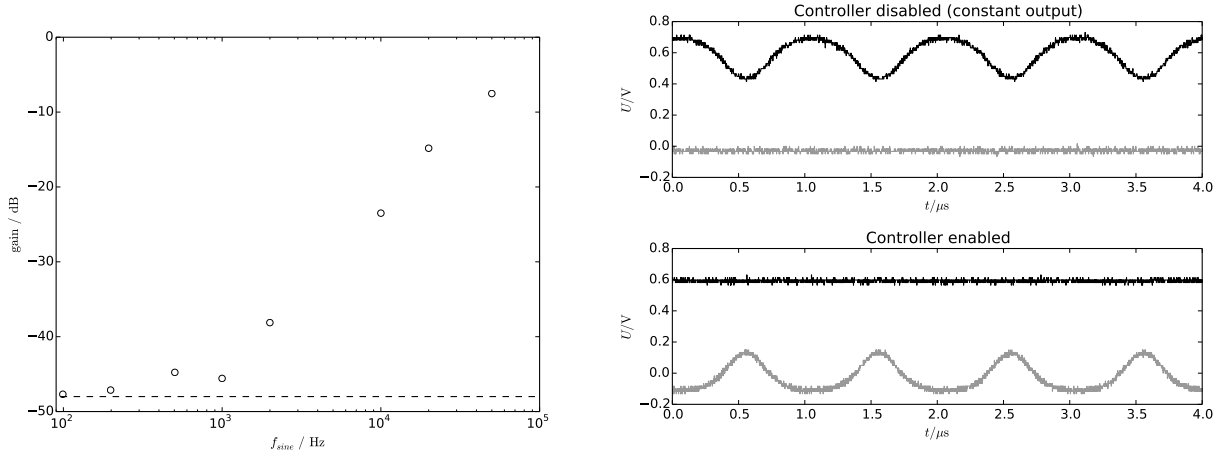


Figure 5.1.: Sine disturbance rejection results of the PI control loop on the 729 nm AOM setup (controller enabled vs. held at constant output). *Left:* Best-case reduction of the “nosie” amplitude reachable at the various disturbance frequencies, with the dashed line denoting the resolution limit of the oscilloscope used for acquiring the data. *Right:* Sample time-domain data at $f_{\text{sine}} = 1 \text{ kHz}$, with the top black lines showing the respective signal of the in-loop photodiode and the bottom gray lines the EVIL output.

measured gain is -14.8 dB , while at $f_{\text{sine}} = 50 \text{ kHz}$ it has reduced to -7.5 dB . Extrapolating this trend, the point where no further reduction can be achieved is around 100 kHz .

This result matches the simulation results discussed in section 4.4 reasonably well. Thus, it is not entirely unreasonable to assume that the improvements Smith prediction offers in the simulation would also be reachable in the experiment, at least to some extent.

5.2. Pulse Shaping Results

The ultimate benchmark for the intensity control loop setup is the effect it has on the qubit operations on the trapped ions – not only because this is the actual target application, but also because a single trapped atom is the most sensitive measurement device available in the laboratory. To this end, two basic experiments were carried out on a trapped calcium ion, with the intensity stabilization loop controlling the 729 nm beam tuned to address the carrier transition. Figure 5.2 shows an overall overview of how the different parts in the 729 nm beam control interact. The AOM used in the setup is an INTRA-ACTION ATM-2001A2 device in double-pass configuration, driven in the same way as described in section 5.1. A THORLABS PDA-36A-EC photodiode was used for feedback, positioned at a pick-off immediately before the beam enters the vacuum system.

A single $^{40}\text{Ca}^+$ ion was loaded into the 3D trap, and cooled near the motional ground state using the Doppler and resolved sideband cooling techniques. In the first experiment, the effect of pulse shaping on the effective frequency spectrum of the carrier pulses was then investigated. For this, the RF frequency of the AOM controlling the beam was scanned around the previously calibrated value for the carrier transition using the control system. For each of the frequencies, a pulse of duration $t_{\text{pulse}} = 20 \mu\text{s}$ was applied to the ion, and the occupation of the $|4^2\text{S}_{1/2}, m = 1/2\rangle$ qubit state determined afterwards. This process was repeated 100 times for each RF frequency, giving an estimate of the state occupation probability.

This sequence was repeated twice, once with a rectangular envelope for the RF signal applied to the AOM, and once for a pulse with a Gaussian envelope (see figure 4.6). The resulting plot of AOM frequency vs. state occupation probabilities is shown in figure 5.2. While caution has to be applied while interpreting the results as the π times for the two experiments were not exactly equal (the intensity of the shaped pulse unfortunately was not calibrated to match the square pulse for

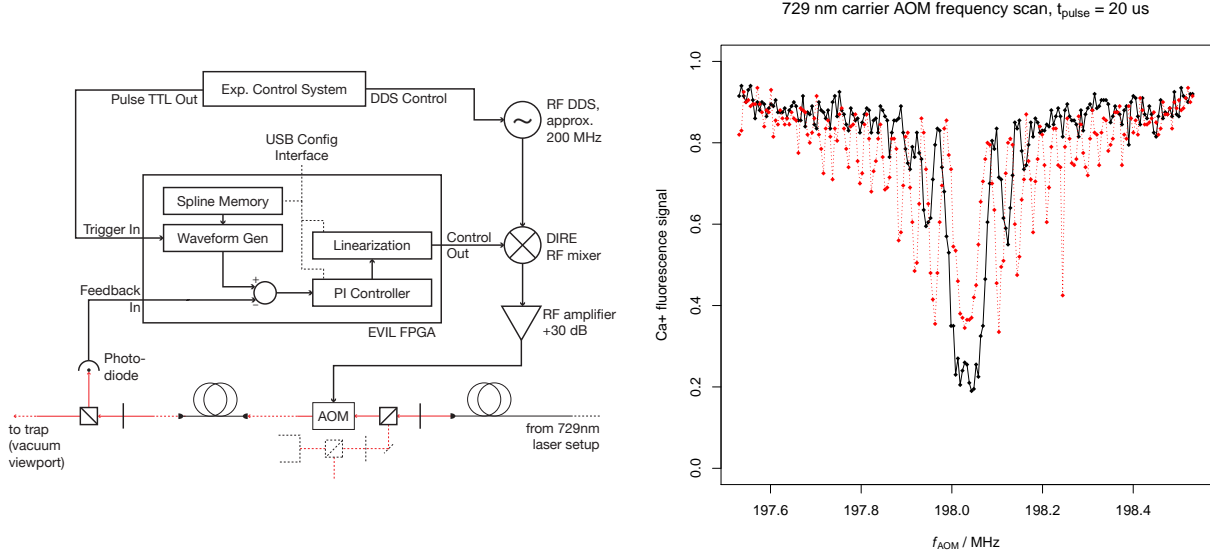


Figure 5.2.: Pulse shaping experiments on the $^{40}\text{Ca}^+$ qubit carrier transition. *Left:* Overall schematic of the intensity stabilization and pulse shaping setup (details of the electrical and optical setups omitted). *Right:* $|4^2\text{S}_{1/2}, m = 1/2\rangle$ qubit state population after applying a 729 nm carrier pulse is shown as a function of AOM frequency (half the laser frequency shift). The results for unstabilized square pulses are shown in red (dotted), the results for a Gaussian-shaped pulse in black (solid).

the given t_{pulse}), it is apparent that the high frequency content in the response is reduced in the pulse shaped case. Qualitatively, this is consistent with the outcome expected from a narrower pulse spectrum, as provided by the Gaussian-shaped edges.

In a second experiment, the AOM frequency was fixed at the carrier transition, but the pulse duration was scanned. Again detecting the qubit state population, it is expected to observe Rabi oscillations, with the contrast (i.e. the amplitude of the oscillations around $p(\downarrow) = 0.5$) decaying towards longer pulse durations due to imperfections in the experimental setup. One such reason for contrast decay would be intensity fluctuations of the gate beam.

In this experiment, no improvement in the contrast decay for the intensity-stabilized pulses over the unstabilized case could be observed.¹ When comparing the pulse shapes (as measured by the in-loop photodiode) on an oscilloscope, it was clear, however, that the controller indeed had a stabilizing effect on the pulse amplitudes.

The most likely explanation for this is that the intensity fluctuations of the beam (and thus the area fluctuations of the gate pulse) simply were not the limiting factor for the Rabi oscillation decay, but other external influences disturbing the energy level structure, e.g. fluctuations in the magnetic field in the trap. The latter is in fact a good candidate for an explanation, because a magnetic field stabilization scheme was being worked on while the measurements were taken.

¹In fact, the decay time for the PI-stabilized case was even slightly worse than for the unstabilized case. This might be attributed to the fact that the sideband cooling scheme could not be run, whereas it was active for the unstabilized runs.

6. Conclusion

In this report, the design, assembly and testing of components for laser pulse shaping centered around accusto-optic modulators for quantum information experiments were described.

A linear RF multiplier circuit was constructed in form of the *DIRE* PCB, and was shown to meet the performance goals. The considerable time delay in the response of the used AOMs was found to be the biggest factor limiting the performance of a simple proportional-integral control loop. Numerical simulations showed results comparable to the actual experiment data. Based on this, more advanced control schemes were investigated, which explicitly compensate for the time delay. The hardware realization of these algorithms was discussed, although the implementations were not actually carried out and/or tested as part of this project.

Measurements on a trapped ion confirmed that pulse shaping indeed contributes to a cleaner effective frequency spectrum of the laser pulses used for manipulating the $^{40}\text{Ca}^+$ qubit state. The closed-loop control could not be shown to have a significant effect on the short-term Rabi flopping contrast decay, although other aspects of stability the trapping setup were greatly improved since the related experiments were performed.

There are three main areas that need further attention on the way to a flexible stabilized pulse shaping setup, but unfortunately could not be investigated as part of the project due to time constraints.

First, the improved control algorithms were simulated numerically, but no time was left to actually implement them on the FPGA-based controller. Whether the improved results from the more complex control schemes can be reached in the experiment is open to question in particular because the model used for the numerical simulations was not very sophisticated. A scheme for compensating for the nonlinearities in the AOM power-to-diffraction-efficiency relation beyond the simple square root function might need to be implemented.

The second missing piece is an investigation of the actual effect of the control loop on the statistical properties of the laser pulse area. This was not pursued beyond the inconclusive Rabi flopping experiment because of the somewhat lackluster set point following and noise rejection performance of the simple PI controller, but would be essential in tracking down the factors limiting operation fidelity in the ion trap setup.

Lastly, further optimizations of the time delay in the response of the used AOMs might be possible by careful alignment and focussing of the laser beams. As such modifications might come at the expense of decreased diffraction efficiency, it might be worth to investigate this after the improved controller has been implemented in hardware, such that the effect on the final noise level can immediately be quantified.

In any case, the presented results should form a solid basis for further investigations concerning laser pulse shaping in our trap setup, particularly because the implementation as a TTL-triggered extension on a separate controller hardware, together with a modular multiplier board, makes it easy to work on the implementation in isolation. If the control loop can be augmented to reliably offer good noise rejection performance, it is envisioned that it will ultimately be integrated into the RF DDS hardware for tighter integration with the main experimental control system.

A. AOM Response Measurements

To verify the assumptions made when modelling the open control loop (consisting of the AOM, the RF source and multiplier, and a photodiode in the first order diffracted beam of the AOM), it was attempted to measure the transfer function of the complete system. The primary target of the investigations was the behavior of the AOM, as the performance of the DIRE RF multiplier has been analyzed in isolation already (see chapter 3), and the photodiode was known to respond fast and linearly enough to not limit the setup.

The transfer function measurement was performed on the AOM setup for the 729 nm carrier beam. To rule out that the long delay measured was caused by the electronics, a dedicated measurement of the RF signal was carried out afterwards in a different AOM setup.

A.1. Open-Loop Frequency Response

To measure the frequency response of the DIRE-AOM-photodiode combination, a DIGILENT *Analog Discovery Kit* was used in Vector Network Analyzer mode, similar to the measurements in section 3.3.4. This time, the DIRE RF multiplier connected to its output was supplied with RF from a TTI *TGR1040* source, and connected to a MINI-CIRCUITS *ZHL-1-2W-S+* RF amplifier. The input of the spectrum analyzer was connected to a THORLABS *PDA-36A-EC* photodiode that is normally used to monitor the laser pulses going into the trap. The optical elements between double-pass AOM setup and the photodiode should not affect the measurement in any way (mirrors, fibers, ...). The peak RF power at the AOM was chosen such that it remained in the linear response region, i.e. far from the saturation limit.

The result of this measurement is shown in figure A.1. The overall envelope of the curves is expected; a fall-off towards higher frequencies due to the finite speed of sound in the crystal and laser beam waist, combined with the exponentially growing phase delay towards higher frequencies due to the constant amount of time the disturbances need to travel from the RF transducers to the beam path.

However, the plot also shows several dips in the gain response, combined with jumps in the apparent phase at the amplitude minima. The first dip occurs at $f = 839$ kHz, and the further drops in apparent amplitude seem to occur around odd multiples of this frequency.

Subsequent time-domain measurements around $f = 800$ kHz revealed that the real behavior of the AOM around this frequency is not represented well by the phase-sensitive detection in the network analyzer. For this, the DIGILENT *Waveforms* device was used in frequency generator mode with the same parameters as used in the previous frequency response measurements. The photo-diode signal was acquired using an oscilloscope.

Figure A.2 shows that as the frequency of the sinusoidal excitation comes closer to $f = 839$ kHz, the response not only drops in amplitude, but a second peak begins to appear in each sine period. It grows in amplitude, until the signal has effectively become sinusoidal at twice the excitation frequency (i.e. at around 1.6 MHz). As the excitation frequency is further increased, one of the peaks decreases in amplitude until a near-sinusoidal signal at the excitation frequency is observed again.

The physical process behind this effect remains unclear. The fact that the phenomenon seems to occur at odd multiples of the base frequency $f = 839$ kHz is reminiscent of standing waves in a

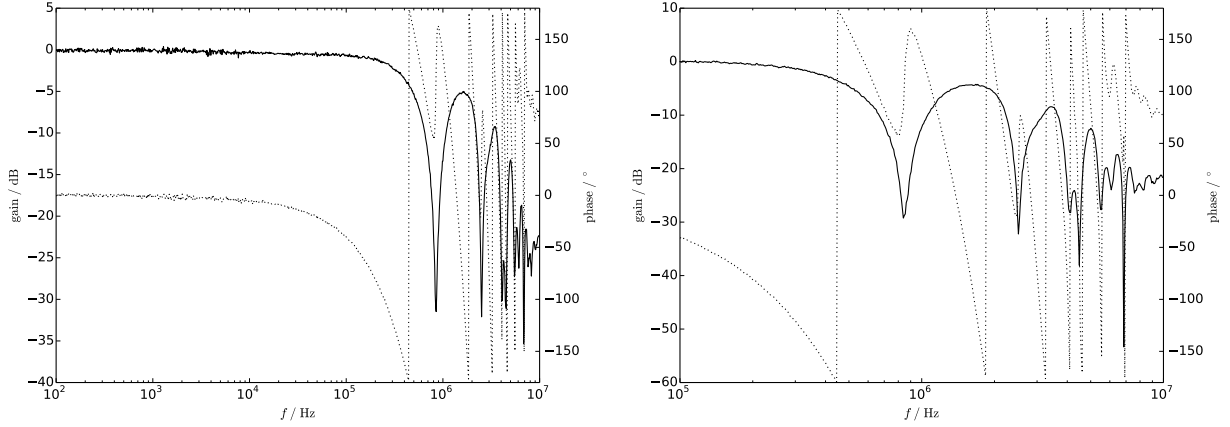


Figure A.1.: Bode plot of the open intensity control loop transfer function, i.e. photo-diode output vs. RF multiplier control input (1000 points). Note the dips around 839 kHz and odd multiples thereof. The right plot shows a slightly higher resolved capture of the interesting region (500 points).

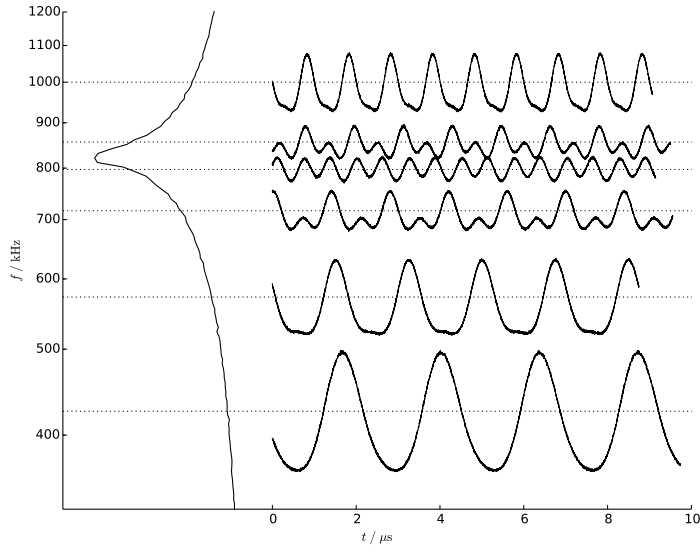


Figure A.2.: Time-domain data corresponding to the first dip in the INTRA-ACTION AOM frequency response curve (figure A.1). On the left, the graph from the network analyzer is shown for reference. The curves on the right represent the photo-diode signals for a sinusoidal excitation at the frequency marked by the dotted lines (arbitrary vertical scale). Note the apparent doubling in frequency near 800 kHz.

mechanical oscillator which is fixed at one end (e.g., an organ pipe). A possible source might be the ultrasonic piezo transducer(s) in the AOM and the incoupling mechanism into the accusto-optic medium (a TeO_2 crystal in this case). A second possible cause might be resonances inside latter medium itself. However, the manufacturer of the AOM, when confronted with the data, could not confirm or deny either of these hypotheses. No attempts to investigate the existence of similar resonance phenomena in other AOM models have been made so far.

Except for this phenomenon, the AOM response seems to be described reasonably well by a time-delay combined with a low-pass filter (note that the AOM was used in double-pass configuration, and thus the considerations in 4.2 regarding the squared amplitude response apply).

A.2. AOM Latency

As further discussed in chapters 4 and 5, the biggest factor limiting the control loop bandwidth is the large phase lag caused by the latency in the response of the accusto-optic modulator. A certain amount of delay is inevitable, as the wave front needs to travel the distance from the piezo transducers to the location of the laser beam in the accusto-optic material. However, the latencies measured in the different AOM setups were generally larger than expected. For example, the INTRA-ACTION *ATM-2001A2* showed a delay time of $\Delta t \approx 1.3 \mu\text{s}$. A simple calculation of the form

$$\Delta x = \Delta t v, \quad \text{where } v = 4260 \text{ m/s (speed of sound in } \text{TeO}_2\text{)}$$

yields a travelled distance of $\Delta x \approx 5.5 \text{ mm}$. While this is compatible with the size of the AOM housing, it still seems larger than expected.

In this calculation, the effect of the electronic control and amplification circuitry is neglected. To ensure that the signal path between the DIRE control input and the AOM does not significantly contribute to the total time delay, a second experiment was performed with the RF signal being monitored directly at the AOM.

For this, an INTRA-ACTION *AOM-802AF3* in single-pass configuration was used, positioned in a setup for 854 nm light at another trap of the group. It showed similar delay characteristics to the AOM in the 729 nm beam path. It was driven using an 80 MHz sine signal generated by a TTI *TGR1040* lab source, controlled by a DIRE board, and amplified using a MINI-CIRCUITS *ZHL-1-2W-S+* RF amplifier to achieve a total power level of 32.5 dBm. Immediately at the AOM RF port, a MINI-CIRCUITS *ZDC-20-1+* directional coupler (-20 dB) was placed. It was connected to a digital oscilloscope, along with the DIRE board control signal and the photodiode output.

Figure A.3 shows the three traces, as captured while applying a full-scale (low-frequency) square wave to the DIRE input port. As expected, an RF signal is detected at the AOM almost immediately after the rising edge of the control signal. The delay of around 100 ns is well within the time scale of latencies in the DIRE input filter, the RF amplifier and the wiring.

Note: The spike in the rising edge of the control signal is just a measurement artifact caused by the fact that the signal was picked off using a BNC T piece without appropriate termination. Also, the RF frequency is much higher in reality than it appears from the middle plot due to heavy aliasing caused by the low sample acquisition rate of the oscilloscope in the timebase used for the measurement.

A manufacturer representative suggested that the latency might be slightly improved at the cost of diffraction efficiency by removing the AOM casing and adjusting the beam closer to the piezo transducers than the aperture in the case permits, thus reducing the propagation time of the mechanical wave. This optimization was not further investigated in the scope of this project (but the beam was carefully aligned to the edge of the aperture in the measurement discussed in section A.1).

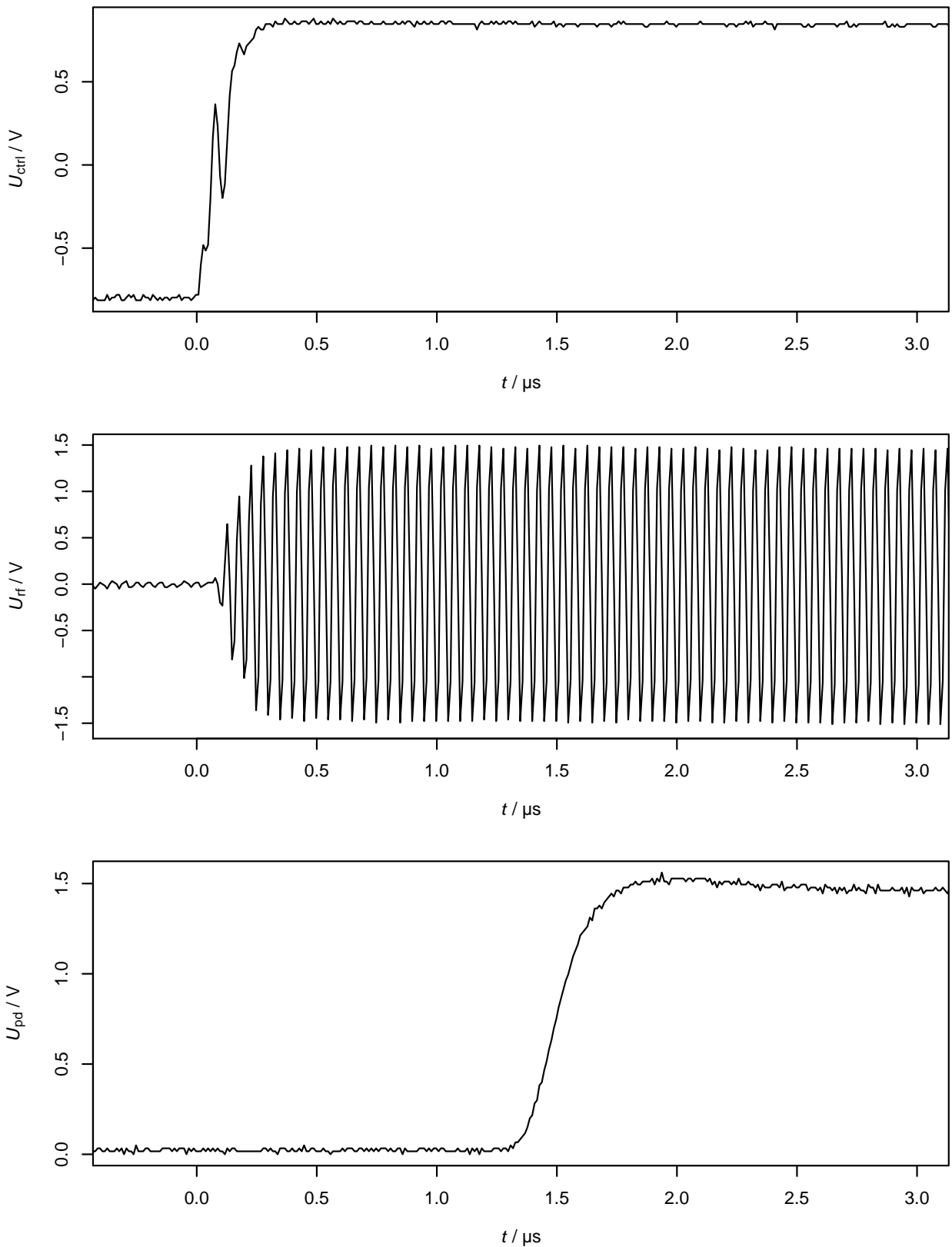


Figure A.3.: INTRA-ACTION AOM-802AF3 switch-on behavior. The top plot shows the control signal going to the RF multiplier (the spike in the rising edge is a measurement artifact). The RF signal at the AOM, as measured via a directional coupler, is shown in the middle plot (note that the capture suffers from heavy aliasing, the RF frequency is about 10 times higher in reality). The bottom graph shows the output of a photodiode positioned in the first-order diffracted beam.

B. DIRE RF Multiplier Assembly and Setup

This section contains details on how to assemble and configure the DIRE RF multiplier board developed as part of this thesis project. Figure B.1 shows the top layer of the PCB, figure B.2 summarizes the input/output characteristics and adjustments, and figure B.3 shows an example of the involved signal levels in a typical setup. The full schematic of the circuit is shown in figure B.4. For the main treatment, please see chapter 3.

B.1. Function Summary

The DIRE board is a voltage-mode device for multiplying an RF signal $V_{\text{rf}}(t)$ by a control voltage $V_{\text{ctrl}}(t)$. Disregarding the input filters, the output voltage can be described as

$$V_{\text{out}}(t) \propto (V_{\text{ctrl}}(t) - V_{\text{offset}}) \cdot V_{\text{rf}}(t),$$

where V_{offset} can be adjusted using a potentiometer on the device.

Figure B.2 summarizes the input/output characteristics. The RF input is AC-coupled (corner frequency: 318 kHz), and a second-order low-pass filter at the control input is used to reduce the susceptibility to noise pick-up. The inputs/outputs are 50 Ω -terminated.

B.2. Configuring the DIRE Board for Use with the EVIL Controller

In the following, a procedure for setting up the DIRE RF multiplier board together with the EVIL controller as part of an AOM-based laser intensity modulation setup is suggested. The optical alignment is not described here, it is assumed that the first-order beam can already be detected at the target photodiode.

If the pulse shaping functionality developed as part of this project is not needed, the standard EVIL firmware can be used for simple PI-based intensity stabilization as well. The instructions will describe the adjustment process for both the default (*DF*) and the pulse shaping (*PSF*) firmware.

1. *Adjust the analog output range of the EVIL:* Set up the EVIL controller and connect its fast DAC output to an oscilloscope. Using the client software, set the output to a full-range ramp (*DF*: sweeping mode with full range; *PSF*: waveform generator in ramp mode and full range, linear output slider at maximum). Then, adjust the potentiometer next to the output socket on the EVIL PCB with a small slotted screwdriver until the peak-to-peak voltage of the signal is around 1.6 V or the lower limit of the output adjustment range is reached, whichever is higher.
2. *Set the DIRE input offset:* Connect the DIRE output to an RF spectrum analyzer and connect the board to a power supply (± 7 to ± 15 V best, up to ± 25 V max.). Ensure that the polarity of the supply is correct, as there is no protection on the board and if it is reversed, the multiplier chip will likely be damaged. Then, set the EVIL output to the most negative voltage (*DF*: set sweep range to zero, offset to minimum; *PSF*: zero all output sliders) and connect it to the DIRE board. Switch on the RF source and minimize the output RF power using the DIRE input offset potentiometer. It should be possible to achieve an attenuation of at least -70 dB.

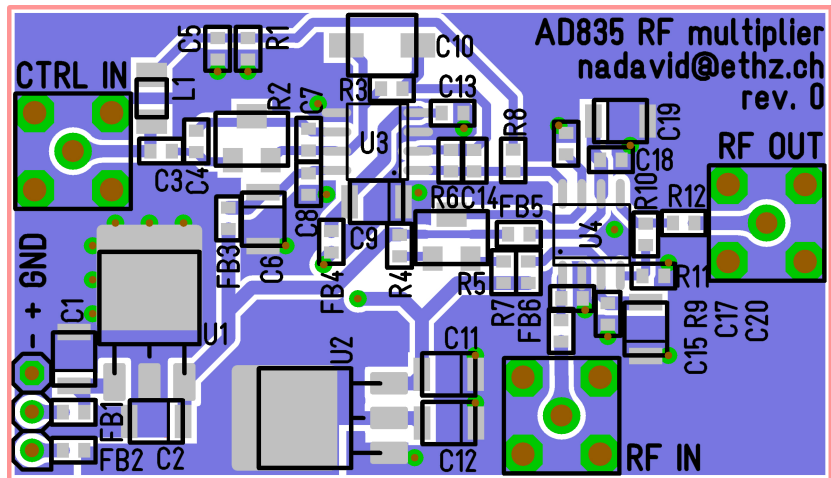


Figure B.1.: Top view of the DIRE RF multiplier PCB layout (scale: 200 %). The bottom copper layer consists of a ground plane, only interrupted by a short negative supply track.

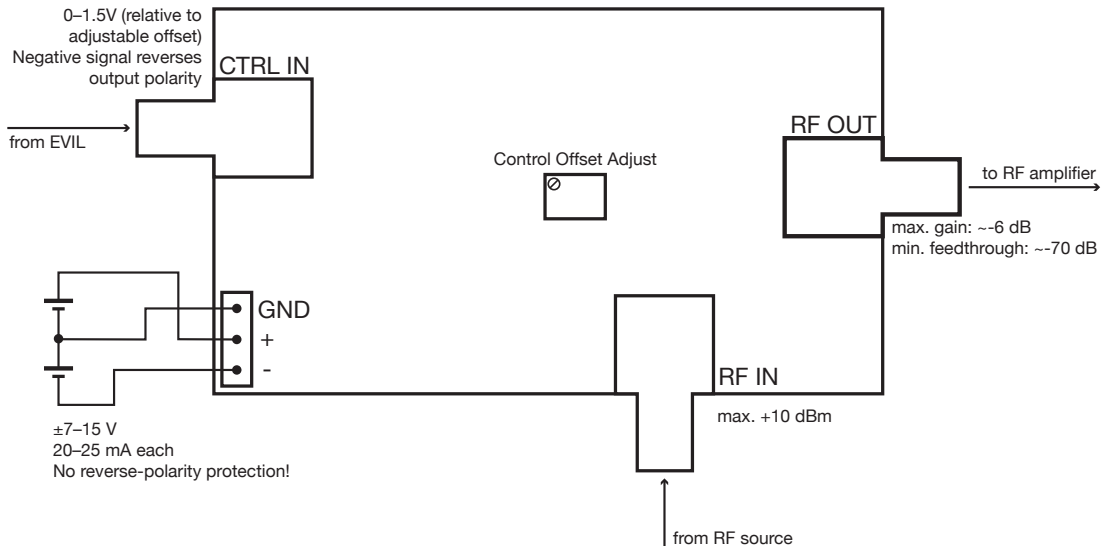


Figure B.2.: Input/output characteristics and adjustments on the DIRE PCB in default configuration (that is, with the fixed-frequency low-pass input filter components populated).

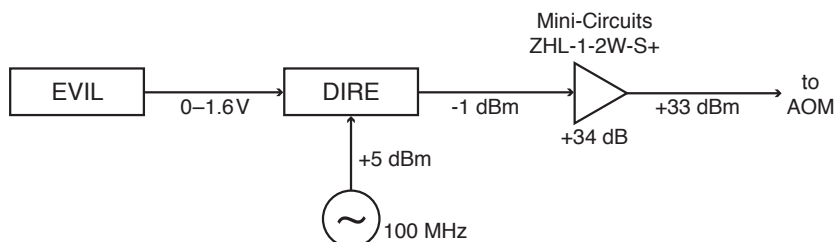


Figure B.3.: Signal levels in a typical setup using the DIRE board for pulse shaping. Note: The required RF power levels vary between different AOM models.

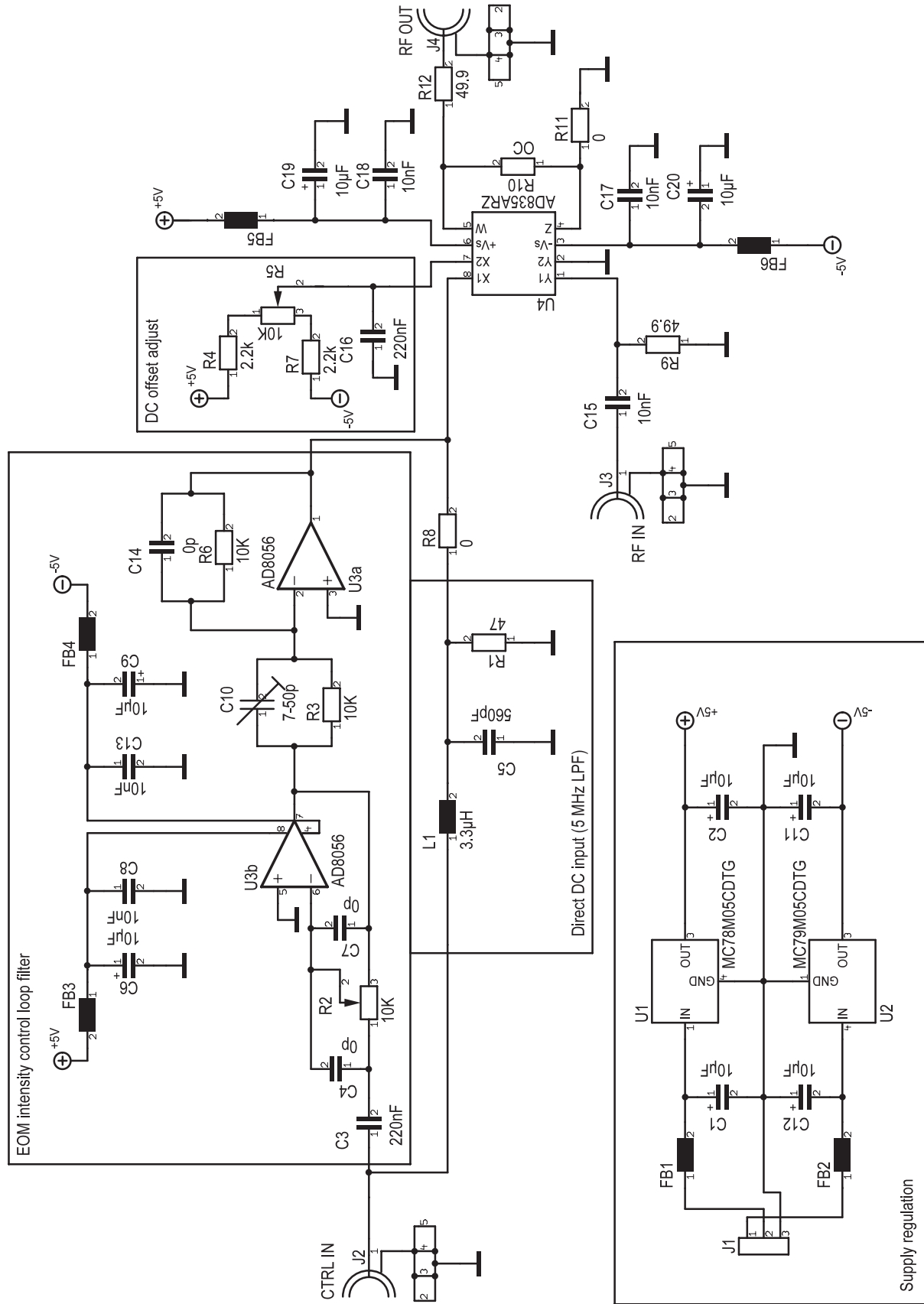


Figure B.4.: DIRE RF multiplier schematic. Capacitors with value “0p” and resistors marked “OC” are not present in the default configuration.

3. *Connect the RF output to the AOM:* Switch off the RF source and disconnect the spectrum analyzer, instead connecting the DIRE output to the RF amplifier that is used to drive the AOM. Before turning on the RF amplifier, make sure that the power levels are suitable for the AOM used. If unsure, connect the spectrum analyzer (with appropriate attenuators inserted!) to the RF amplifier in place of the AOM and power up the RF amplifier, verifying the power levels by manually setting the EVIL output to maximum (*DF*: sweeping mode, max. offset; *PSF*: set output offset to max.). (Re)connect the RF amplifier to the AOM, switch on its power supply and (re)enable the RF source.
4. *Verify/adjust the photodiode gain:* Connect the photodiode to an oscilloscope, set the EVIL output to maximum, and verify the signal levels, resp. choose the gain appropriately for variable-gain photo-diode detectors. The optimal level is a trade-off between the bandwidth of the amplifiers in the detector (or other external amplifiers) used, the range of the EVIL analog frontend (i.e. ADC resolution and noise), and of course the fraction of the light being available for feedback. For the tests conducted as part of this project, a photodiode signal level of around 1 V at full laser intensity was used as a compromise, with the gain on the Thorlabs PDA-36A photodetector set to 20 dB.
5. *Adjust EVIL analog input gain:* Connect the photodiode to EVIL input A and adjust the input gain potentiometer (on the EVIL PCB, near the corresponding SMA input jack) based on the streaming view in the EVIL software (the ADC range being ± 512). The new overrange detection feature is useful to immediately recognize overflow conditions in the running system (and also in the logs for post-mortem diagnosis), allowing you to keep the headroom small to make best use of the 10 bits of ADC resolution.
6. *Verify/adjust digital EVIL output range (PSF only):* The actual clipping range of the AD835 multiplier chip on the DIRE board varies slightly between different chips, so it is useful to verify the behavior across the whole range by generating a full-range sweep and monitoring the photodiode response (using the streaming function or an oscilloscope in parallel to the EVIL input). As the sweep range of 1.6 V set in step 1 is larger than the typical clipping range of 1.4 V (as per the AD835 data sheet), slight clipping will likely be visible at the top end. The pulse shaping firmware additionally supports fine-tuning the output range to avoid this. To do so, simply adjust the linear (single pass AOM) or square root (double pass AOM) output slider such clipping is no longer visible.

Bibliography

- [1] C. Monroe and J. Kim, Science **339**, 1164 (2013).
- [2] D. Leibfried, R. Blatt, C. Monroe, and D. Wineland, Rev. Mod. Phys. **75**, 281 (2003).
- [3] K. Fisher, “Coherent Control Laser System for the Quantum State Manipulation of Trapped Ions”, MSc thesis (ETH Zürich, Department of Physics, 2013).
- [4] A. H. Burrell, D. J. Szwier, S. C. Webster, and D. M. Lucas, Phys. Rev. A **81**, 040302 (2010).
- [5] K. Mølmer and A. Sørensen, Phys. Rev. Lett. **82**, 1835 (1999).
- [6] B. Saleh and M. Teich, *Fundamentals of photonics*, Wiley Series in Pure and Applied Optics (Wiley, 2007) Chap. 20, pp. 799–831.
- [7] E. H. Young Jr. and S.-K. Yao, Proceedings of the IEEE **69**, 54 (1981).
- [8] E. A. Donley, T. P. Heavner, F. Levi, M. O. Tataw, and S. R. Jefferts, Review of Scientific Instruments **76**, 063112, pages (2005).
- [9] Texas Instruments, *MPY634: Wide Bandwidth Precision Analog Multiplier (Rev. A)*, (Dec. 2004) <http://www.ti.com/lit/gpn/mpy634>.
- [10] Analog Devices, *AD834: 500 MHz Four-Quadrant Multiplier (Rev. F)*, (2012) http://www.analog.com/static/imported-files/data_sheets/AD834.pdf.
- [11] Analog Devices, *AD835: 250 MHz, Voltage Output, 4-Quadrant Multiplier (Rev. D)*, (2012) http://www.analog.com/static/imported-files/data_sheets/AD835.pdf.
- [12] Analog Devices, *ADL5391: DC to 2.0 GHz Multiplier*, (2012) http://www.analog.com/static/imported-files/data_sheets/ADL5391.pdf.
- [13] P. Horowitz and W. Hill, eds., *The art of electronics*, 2nd (Cambridge University Press, 1980).
- [14] H. Wheeler, IEEE Transactions on Microwave Theory and Techniques **25**, 631 (1977).
- [15] Schmitz, Tamara and Wong, Mike, *Choosing and Using Bypass Capacitors*, (2011) <http://www.intersil.com/data/an/an1325.pdf>.
- [16] Ardizzone, John, Analog Dialogue **39-09** (2005).
- [17] C. Brown and D. J. Coombs, *Technical Report 387: Notes on Control with Delay* (The University of Rochester, Aug. 1991).